**T.R.**
**GEBZE TECHNICAL UNIVERSITY**
**INSTITUTE of EARTH and MARINE SCIENCES**

# EARTQUAKE FOCAL MECHANISM ANALYSIS of THE GULF of GÖKOVA and ITS SURROUNDINGS

**EDANUR TANÜLKÜ AL JASIM**
**THESIS SUBMITTED for THE DEGREE of MASTER of SCIENCE**
**DEPARTMENT of EARTH and MARINE SCIENCES**

**GEBZE**
**2023**

**T.R.**

**GEBZE TECHNICAL UNIVERSITY**

**INSTITUTE of EARTH and MARINE SCIENCES**

# EARTQUAKE FOCAL MECHANISM ANALYSIS of THE GULF of GÖKOVA and ITS SURROUNDINGS

**EDANUR TANÜLKÜ AL JASIM**

**THESIS SUBMITTED for THE DEGREE of**

**MASTER of SCIENCE**

**DEPARTMENT of EARTH and MARINE SCIENCES**

THESIS SUPERVISOR

Asst. Prof. Dr. DİĞDEM ACAREL

**GEBZE**

**2023**

**T.C.**

**GEBZE TEKNİK ÜNİVERSİTESİ**
**YER ve DENİZ BİLİMLERİ ENSTİTÜSÜ**

# GÖKOVA KÖRFEZİ ve YAKIN ÇEVRESİNİN DEPREM ODAK MEKANİZMASI ANALİZİ

**EDANUR TANÜLKÜ AL JASIM**
**YÜKSEK LİSANS TEZİ**
**YER ve DENİZ BİLİMLERİ ANABİLİM DALI**

DANIŞMANI
Dr. Öğr. Üyesi DİĞDEM ACAREL

**GEBZE**
**2023**

| GEBZE TEKNİK ÜNİVERSİTESİ | YÜKSEK LİSANS JÜRİ ONAY FORMU |
|---|---|

GTÜ Yer ve Deniz Bilimleri Enstitüsü Yönetim Kurulu'nun 24/01/2023 tarih ve 2023/03 sayılı kararıyla oluşturulan jüri tarafından 27/01/2023 tarihinde tez savunma sınavı yapılan Edanur TANÜLKÜ AL JASIM'ın tez çalışması Yer Bilimleri Anabilim Dalında YÜKSEK LİSANS tezi olarak kabul edilmiştir.

**JÜRİ**

ÜYE
(TEZ DANIŞMANI) : Dr. Öğr. Üyesi Diğdem ACAREL

ÜYE : Doç. Dr. Hakkı BALTACI

ÜYE : Prof. Dr. Bülent KAYPAK

**ONAY**

Gebze Teknik Üniversitesi Yer ve Deniz Bilimleri Enstitüsü Yönetim Kurulu'nun ...…/…../…… tarih ve ……/…..... sayılı kararı.

İMZA/MÜHÜR

In Loving Memory of My Beloved Mom

# SUMMARY

The Gulf of Gökova, located in the W Anatolian horst graben system, is one of the seismically most active regions in Turkey. The Gökova Fault Zone (GFZ) is developed alongside several complex features due to plate motions along the Aegean subduction zone. The region has experienced intense seismic activity both in historical and instrumental periods. Particularly, following the 2017 Mw6.6 Bodrum earthquake, the complicated tectonic structure of the region was studied extensively and highly debated indicating the necessity of a detailed study of the active tectonics of the region.

In this study, source parameters of 140 earthquakes (M>3.0) occurred between 2006-2022, in and around the Gulf of Gökova (located between 36.5°-37.5°N and 26.8°-29°E), are calculated to be further implemented in stress tensor inversion. The region is divided into six sub-regions concerning depth, focal mechanism variations, and active tectonic features. In the northern part of the gulf, including the Gökova and Muğla faults, the maximum principal stress indicates normal faulting, with a counter-clockwise motion from NW-SE to NE-SW. The southern part of the gulf exhibits scattered seismicity and diverse tectonic elements, including Datca, Bozburun, Selimiye and Taşlıca faults. Hence, the observed principal stresses indicate a transformational structure that concurrently induces normal and strike-slip faulting.

**Key Words: The Gulf of Gökova, Earthquake Focal Mechanism Solution, Stress Analysis, Seismotectonic**

# ÖZET

Batı Anadolu horst-graben sistemi içinde bulunan Gökova Körfezi, deprem etkinliği bakımından Türkiye'nin en aktif bölgelerinden biridir. Bu etkinlik, Ege Yitim Zonu boyunca gelişen levha hareketlerinin bir sonucu olarak meydana gelmiş olan başta Gökova Fay Zonu (GFZ) olmak üzere bölgedeki farklı fay sistemlerinin hareketi sonucu ortaya çıkmaktadır. Gökova Körfezi'nin içinde bulunduğu bölgede, tarihsel dönemlerde ve aletsel dönemde büyük depremler meydana gelmiştir. Bölgenin karmaşık yapısı güncel depremler nedeni ile yapılan çalışmalarda tartışılmış ve bölgede aktif olan tektonik gerilmenin ayrıntılı analizini yapma gerekliliğini doğurmuştur.

Bu çalışmada, 36.5°-37.5° K enlemleri ile 26.8°-29° D boylamları arasında kalan Gökova Körfezi ve yakın çevresinde 2006-2022 tarihleri arasında üç bileşenli geniş bantlı sismometreler ile kaydedilen, M≥3.0 büyüklüğündeki 140 depremin moment tensör ters çözüm yöntemi ile kaynak parametreleri elde edilmiştir. Elde edilen odak mekanizması çözümleri bölgeyi daha detaylı incelemek amacıyla stres tensörü ters çözümünde kullanılmış ve aktif gerilme alanları belirlenmiştir. Bölge, odak mekanizması değişimi, derinlik ve tektonik unsurlara göre 6 alt bölgeye bölünmüştür. Alt-bölgeler için yapılan stres analizi, Gökova Fay Zonu ve Muğla Fayını içeren körfezin kuzey kısmı boyunca, maksimum asal gerilmenin ($\sigma_1$) KB-GD'dan KD-GB'ya batıya doğru saat yönünün tersine değiştiğini ve normal faylanma rejiminin etkin olduğunu göstermiştir. Öte yandan, körfezin güney kısmını oluşturan Datça, Bozburun, Selimiye ve Taşlıca Faylarını içeren kısım dağınık sismisite ve tektonik karmaşıklık göstermekte asal gerilme yönleri, doğrultu atımlı faylanmayı ve normal faylanmayı eş zamanlı üreten bir transformasyonel rejim göstermektedir.

**Anahtar Kelimeler: Gökova Körfezi, Deprem Odak Mekanizması Çözümü, Gerilme Analizi, Sismotektonik**

# ACKNOWLEDGEMENTS

First of all, I would like to express my sincere gratitude to my advisor, Dr. Diğdem Acarel, for her unwavering support, constant advice, insightful criticism and time during my studies.

Prof. Dr. Bülent Kaypak deserves my heartfelt thanks for his invaluable advice and guidance, as well as his never-ending patience throughout my studies.

Furthermore, I am deeply grateful to Prof. Dr. Gürol Seyitoğlu and Dr. Begüm Koca for their patience to my never-ending questions and guidance throughout my thesis.

This thesis is completed as a part of and partially supported by the project UDAP-Ç-19-20. I am grateful for the help and support of the project team, especially Burcu Güvenli and Tuğçe Bilgiç.

Last but not least, there is a special person without whom I would not be able to complete this journey, my beloved Dr. Omar Aljasim.

# TABLE of CONTENTS

# LIST of ABBREVIATIONS and ACRONYMS

| **Abbreviation and Acronyms** | | **Explanations** |
|---|---|---|
| **GofG** | : | The Gulf of Gökova |
| **FMS** | : | Focal Mechanism Solution |
| **MT** | : | Moment Tensor |
| **DC** | : | Double Couple |
| **CLVD** | : | Compensated Linear Vector Dipole |
| **NOA** | : | Institute of Geodynamics-National Observatory of Athens |
| **KOERI** | : | Boğaziçi University Kandilli Observatory and Earthquake Research Institute-Regional Earthquake-Tsunami Monitoring Center (KOERI-RETMC) |

# LIST of FIGURES

# LIST of TABLES

# 1. INTRODUCTION

Determination of the earthquake focal mechanism is one of the most fundamental tool seismologists use to explore the nature of the stresses associated with an earthquake, in general terms the active tectonic setting. There are several approaches to calculate focal mechanism solutions: first motion of P waves, study of P/S amplitude ratios and polarization, amplitude of S waves, and moment tensor inversion. These approaches make use of the seismic wave radiation pattern, which expresses the fault orientation and slip direction during an earthquake. Nowadays, the earthquake size and geometry are deciphered by calculating the seismic moment and moment tensor more effectively. In this study, in order to elaborate on the seismotectonic setting of Gulf of Gökova, the source parameters of the earthquakes between the years of 2006-2022 are determined and the characteristics of the earthquake and fault structures are revealed utilizing a time domain moment tensor inversion and stress inversion methods.

The Gulf of Gökova lies between the Bodrum and Datça peninsulas in SW Turkey, with a length of 100 km in EW direction and a width of 20 km NS direction. It is one of seismically most active regions in Turkey due to its critical location in the Western Anatolian horst-graben system in which an element of Aegean subduction zone, Gökova Fault Zone (GFZ), exists. The latest major earthquake (Mw=6.6) occurred near Bodrum on 20 July 2017 (22:31:00 UTC) followed by thousands of aftershocks.

Due to its tectonically complex structure and active seismicity, various geophysical and seismological studies have been carried out in the region both onshore and offshore. Tezcan and Turgay [1991], suggested that the heat flux in the Gulf of Gökova varies between 120 – 80 $mW/m^2$ from northwest to southeast. Using gravity and magnetic field data, Göktürker et al. [2003] attempted to determine the two-dimensional thermal field in the Muğla-Yatağan half-graben crust. Aydın et al. [2005], using the airborne magnetic data collected by the MTA between 1978 and 1989, it was determined that the depth of the Curie point is 18-22 km to the west of the Fethiye-Burdur Fault Zone extending in an arc shape toward the island of Crete. The heat flux in the Gulf of Gökova has been calculated to be between 85-100 $mW/m^2$. In Karayel et al. [2009], gamma spectrometric analysis of sand samples

taken from the coastline was performed in the laboratory to determine the radioactivity levels on the Bodrum–Turgutreis coast. According to Akın and Üçer [2013], anomalies in the gulf indicate that the ultrabasic, ophiolitic melange (complex) of the Gulf Datça is also present in the Gulf of Gökova. Based on the data, the northern boundary of the peridotite is thought to be approximately nine kilometers closer to the northern boundary of the Gulf. Akın et al. [2014] calculated the depth of the Curie point by using the airborne magnetic data of Turkey and found the heat flux value between 55 – 75 $mW/m^2$ in the Gulf of Gökova. The effects of the African–Aegean–Anatolian Subduction Zone and the Aegean Volcanic Arc were studied by geothermic methods in Erbek [2018], a study conducted on the Bodrum peninsula to determine the thermal structure of South-Western Anatolia. Çağlar and Duvarcı[2001], applied the vertical electrical sounding method at 61 points on land in the Gulf of Gökova using the Schlumberger method, which is less sensitive to lateral changes. Düztaş et al. [2017] used electrical resistivity tomography and induced polarization method together around Muğla Province.

Using seismic reflection data, Günay [1999] studied the tectonic properties of the Saros, Edremit, and Gökova gulfs, which shape the Western Anatolian coasts and have a “V”-shaped geometry toward the west. Kurt et al. [1999] obtained detailed information about the tectonic elements of the gulfs of Gökova and Saros by reprocessing the multichannel seismic reflection data collected in 1996. In addition, bathymetric and topographic changes in and around the gulfs were mapped and associated with seismic reflection profiles. Kaşer [2004] investigated the current tectonics of the Gulf of Gökova with studies on high resolution 3.5 kHz and 800 km single channel seismic reflection profiles. Evren [2019] aimed to reveal the stratigraphy of the tectonic structure with the formation of the active faults of the gulf with the multi-channel seismic reflection data of the Gulf of Gökova.

Eyidoğan et al. [1996] determined that the eastern part of the Gulf of Gökova was seismically more active and detected earthquake activity extending between İstanköy (Kos) Island and the eastern part of the gulf. It has been observed that seismic activity is intense along the Ören coast and in the region between Yatağan-Milas-Yerkesik. It is thought that this activity is related to the Ula-Ören fault zone and the Muğla-Yatağan fault zone. It has been determined that the seismogenic zone in the Gökova Basin region is located in the upper parts of the earth's crust and its depth descends to a depth of up to 15 km from the earth's surface.

In Aktar et al. [2006], Moho depth information of the region is obtained using receiver function method. In this study, similar to the results of Eyidoğan et al. [1996], it was determined that the earthquake activity occurred on the active faults called the GFZ along the northern border of the gulf. Based on the distribution of earthquakes here, they proposed a model in which the GFZ is three-segmented. However, they did not observe any significant activity on the southern border of the gulf (except in the western area). In terms of the deep crustal structure, a normal continental crust image with a thickness of 25-30 km was obtained for the north of the GofG, while the Moho discontinuity could not be clearly observed in the southern part. This feature, which is unique to the south of the gulf, has been associated with the Aegean Subduction process. The inability to display the Moho in the southern formations has been interpreted as excessive serpentinization due to the subducting plate.

Sayıl and Osmanşahin [2008], studied the seismicity of W Anatolia, they calculated the Gutenberg-Richter magnitude frequency relationship, seismic risk, and recurrence time. The highest b values are are determined for Demirci-Gediz and GofG-Muğla-Gölhisar. The lowest b values were determined in Balıkesir and Bodrum-İstanköy. Finally, seismic risk and recurrence time calculations from a and b values showed that the subregions with the lowest b values, the highest risk, and the shortest recurrence periods Balıkesir and Bodrum-İstanköy, as expected.

Yolsal-Çevikbilen, et al. [2014], obtained models of the source mechanism parameters of earthquakes occurring in the Gulf of Gökova, the rake distribution, and rupture processes. It is determined that earthquakes generally occur at shallow focal depths, have a normal E-W fault mechanism, and have a very small amount of strike-slip fault components in the focal mechanism solutions. Tsunami wave simulations were developed for historical earthquakes, showing that an earthquake in the region may cause significant tsunami waves mostly in areas close to the epicenter, for example, on the island of Rhodes and around it, and on the shores of the GofG-Fethiye.

Rontogianni et al. [2011] investigated shallow earthquake activities in the GofG. The location of the earthquakes showed that the seismic activity spread from İstanköy (Kos) Island to the center of the gulf, mainly in the south of the gulf. Seismic activity has been observed at depths ranging from 5 km to 15 km from the west of the gulf to the interior of the gulf. These observations show that the activity

of the Datça Fault has not slowed down. Kılıç and Kalyoncuoğlu [2017], focused on the current seismicity in western Anatolia in their study. As a result of the calculations, it was found that the "mmax" value that may occur in the region is between $6.0 \leq M_w \leq 6.5$. At a later stage of the study, the faults that are likely to produce earthquakes (Karaova-Milas Fault, Muğla-Yatağan Fault, and Ula-Ören Fault) and the earthquake parameters of these faults were determined. The moment magnitudes of the faults in the region were calculated using geometric properties and seismogenic layer thicknesses and found to be between 5.9–6.9 [21]. The İstanköy (Kos) Fault, which exhibits significant seismicity activity at different periods of the study, has the potential to produce the largest earthquake in the Southeastern Aegean Region with a moment magnitude of 6.9.

This thesis consists of five chapters. Following the introduction part, thesis continues with Chapter 2 which is an overview of the regional tectonic setting and seismicity of the area. In Chapter 3, the moment tensor analysis is explained in detail. Chapter 4 presents the stress inversion using STRESSINVERSE software developed by Vavryčuk [2014] which is followed by a discussion section in Chapter 5.

# 2. TECTONIC SETTING AND SEISMICITY

Turkey is located in the Alpine-Himalayan orogenic belt at the intersection of the Arabian, African and Eurasian plates. About 12 million years ago, the Arabian plate and the Eurasian plate collided, and in the advanced stage of the collision, the North Anatolian Fault (NAF) and East Anatolian Fault (EAF) zones, which form a conjugate fault system, occurred in the north of the collision zone. Along these left and right lateral strike-slip faults, the Anatolian microplate began to move westward [23]-[26]. The rotation of the Anatolian microplate is counterclockwise as it escapes westward movement rate of 35 mm/year [27], [28]. The map of major tectonic structures of the Anatolian microplate is shown in Figure 2.1.

During the current tectonic process of the region, the Eastern Anatolian region between the Caucasus and the Bitlis Zagros suture zone is undergoing deformation under the north-south compressional tectonic regime. Under this tectonic regime, the current crustal deformation in eastern Anatolia is covered by faults of different geometries and mechanisms [26]. In Central Anatolia, between the eastern Anatolian compressional and western Anatolian compressional tectonic regimes, a complex deformation is observed with strike-slip, normal and reverse faults.

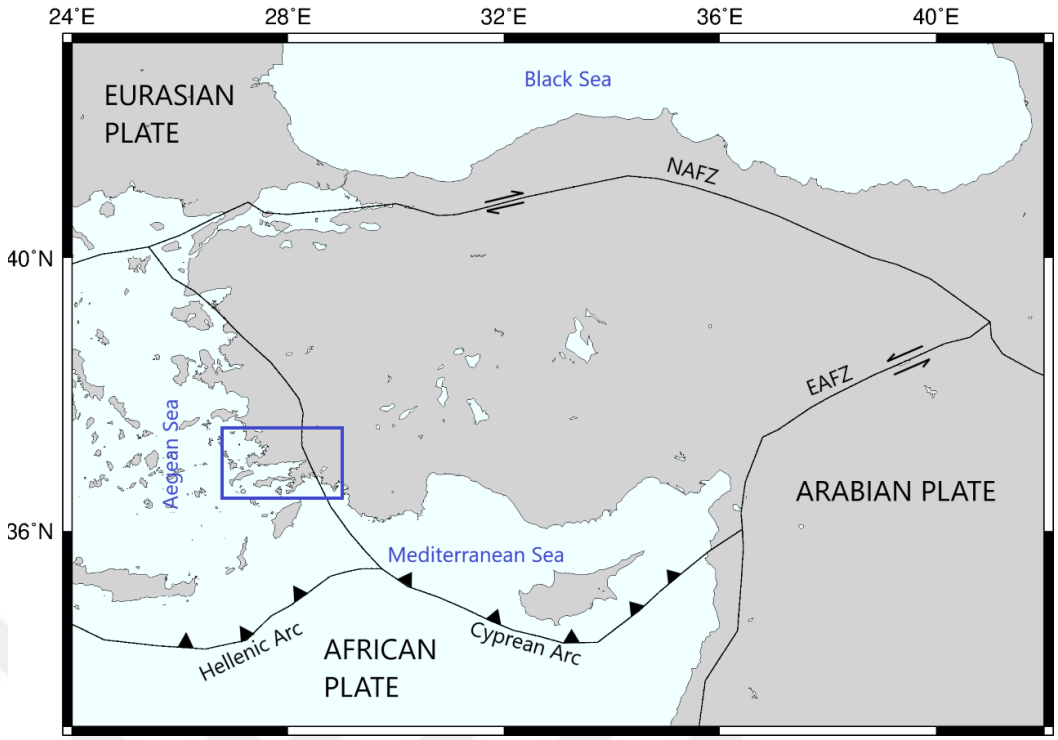


Figure 2.1: The major tectonic structures of Turkey. Black lines with black triangles represent trenches. EAFZ: East Anatolian Fault Zone, NAFZ: North Anatolian Fault Zone. The study area is outlined by blue box.

The Anatolian microplate, which moves westward along the NAF and EAF zones, rotates counterclockwise and is pushed over the oceanic African plate in the SW direction in the Aegean-Cyprian subduction zone [23], [29], [24], [26], [30]. This situation also controls the continental extension tectonics in western Anatolia [31]-[33]. This neotectonic process in western Anatolia is characteristic of the east-west trending horst-graben structures, which define the north-south extension.

In addition to the NAF and EAF transform faults, which provide the westward escape of the Anatolian plate and play an important role in the kinematics of the Eastern Mediterranean region, Aegean extensional system also controls the seismicity of the region around Turkey.

The western Anatolian horst graben system is one of the fastest expanding areas of its type in the world with a speed of 20 mm per year [34]-[44]. This aspect leads to a significant amount of seismic activity in the area, and therefore, moderate and large earthquakes occur frequently. The region is located within the Aegean extension area formed on the subducting African plate [43]. It is defined as a sub-area within the Western Anatolian extension proposed by [26].

The origin of continental expansion in the Aegean region has been debated and different views have been put forward. One of these views is the tectonic escape model, which is explained by the movement of the Anatolian block continuing to the west due to the compression in the east [24]-[26], [45], [46], [43]. The second view argues that the extension in the Aegean region occurred due to the regression of the Aegean Arc system (back-arc spreading model) [29], [47], [48]. However, there is no consensus on the onset of arc regression, suggesting a rather wide time interval (60-5 Ma) [29], [31], [47]-[49]. Another view is that the extension in the Aegean region developed due to the orogenic collapse. Another view is that the extension in the Aegean region developed due to the orogenic collapse in Late Oligocene and Early Miocene [50], [51]. According to the last view, the extension in the region occurred with a two-stage grabenization. The first of these occurred in the Miocene-Early Pliocene period due to orogenic collapse, and the other in the Plio Quaternary period, which developed due to the tectonic escape model [26], [45], [52]- [56].

## 2.1. Active Tectonic Setting of the Gulf of Gökova

Studies reveal that the east-west trending rift system linked to active normal faulting in the Gökova region [57], [46], [12], [58]. In some places, these faults cross each other [32]. Normal faults of different widths and dips define the rift system. One notable fault in the region is the Gökova fault zone, which created the modern gulf system in western Turkey and defines the northern edge of the Gulf of Gökova. The northern margin has more extensive and continuous faults than its southern margin pointing to a listric character. The north-dipping Datça fault, an EW-trending subsurface active listric fault connected to several minor antithetic faults, forms the southern limit of the gulf [12]. Several more faults have also been discovered in the Gulf region through comprehensive bathymetric and seismic studies [46]. Figure 2.2 resembles the active tectonic setting of the Gulf of Gökova, fault data taken from Emre et al., [2013].

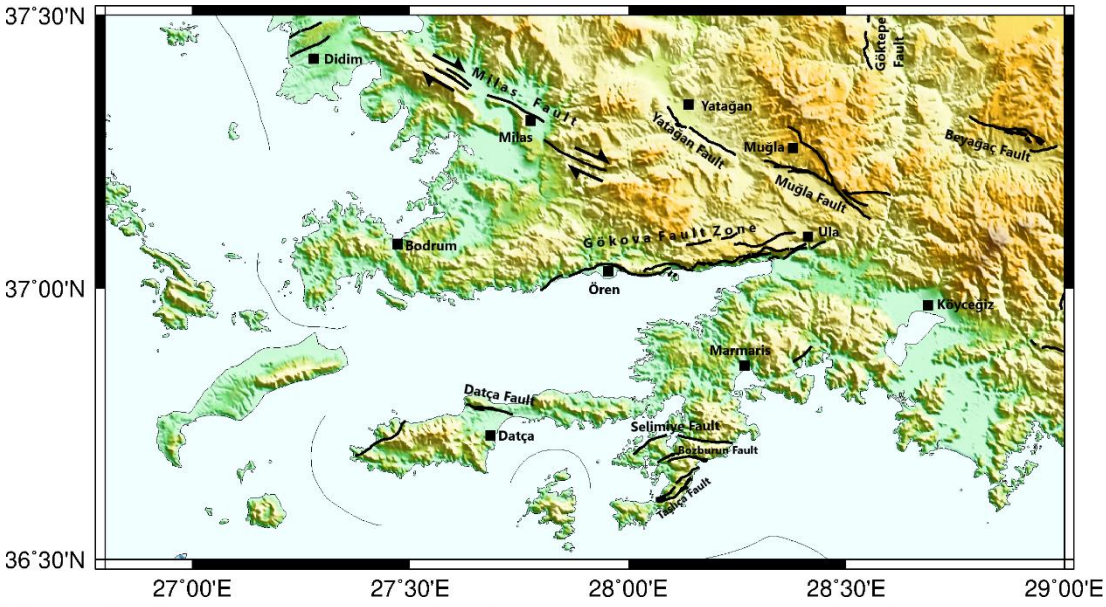


Figure 2.2: Active faults (black,bold lines) in the Gulf of Gökova.

### 2.1.1. Muğla and Yatağan Faults

Although the Muğla and Yatağan faults are mapped as right-lateral strike-slip faults zone so called as Muğla-Yatağan Fault Zone [59], in later published studies, they are shown as normal faults with a NW-SE direction, with a SW and NE dip [60], [61] .

Gürer et al. [2013] mapped the Muğla and Yatağan faults and emphasized the SW edge of the Muğla graben as a fault, stated that the Yatağan fault is an oblique normal fault with a right lateral component. Based on the structural data at a location of the Muğla Fault, it has been claimed that the right-lateral strike-slip fault was obducted by normal faulting. The characteristics related to the Muğla faults were discussed and the distribution of segments belonging to this fault was proposed and a seismic activity has been dated to the year 6000 BC. [63], [64]. Karabacak [2016] stated that the Yatağan Fault has an oblique normal character. The structural data presented by Basmenji et al. [2021] show that the Yatağan Fault meets the NE-SW expansion. In addition, with the data collected from two paleoseismological trenches opened on this fault, and it has been stated that earthquakes occurred on the date 366-160 BC and. 342±131 BC.

### 2.1.2. Gökova Fault

Geological map of the Gökova graben is presented in the article of Görür et al. [1995], as expansion under the control of normal faulting on the northern edge.

In the active fault map of Turkey, the normal faults in the north of the GofG are referred to as the “Ula-Ören Fault Zone” [59]. Later, it was revised and renamed as “Gökova Fault Zone” [61]. The recent maps of the Gökova Fault are detailed in Akyüz et al. 2019 [64].

The bathymetry and seismic reflection studies of the Gulf of Gökova were used to identify the submarine faults [66]-[69]. Uluğ et al. (2005) and İşcan et al. (2013) defined a NE-SW trending fault zone in the gulf.

Numerous articles have been published on the seismicity mainly indicating normal faulting [18]. Subsequent to the 2017, (Mw=6.6 Bodrum-Kos) earthquake, studies have been multiplied, mostly focusing on the fault plane; whether it is a north dipping normal fault [70]-[72] or a south dipping normal fault [73], [74].

### 2.1.3. Datça, Bozburun, Selimiye and Taşlıca Faults.

Datça, Bozburun, Selimiye and Taşlıca faults are the active tectonic elements of the Gulf of Gökova that cover the southern part of the region. The Datça Fault, is a NE-SW trending northward dipping listric normal fault bounding the graben located in the southern of GofG [12]. Bozburun, Selimiye and Taşlıca faults are located in the Bozburun peninsula with normal fault characteristics.This active faulting indicates that the Bozburun Peninsula extends in a north and northwest direction similar to the rest of SW Turkey [60].

## 2.2. Seismicity of the Gulf of Gökova

In this section, seismicity observed in the GofG is summarized both for historical and instrumental periods. Moreover, an analysis of the seismicity since 1900 is presented.

### 2.2.1. Historical Seismicity

The W Anatolia and the Aegean Sea have been seismically active in the past. Historical catalogs, based on historical information, documents, and artifacts, are essential to shed light on the past seismicity of a region. Depending on these catalogs, the distribution of the most destructive historical earthquakes in the Gulf of Gökova and its surroundings for the years BC 5 – AD 1900 are shown in Figure 2.3 and listed in Table 2.1. Many destructive earthquakes occurred in the Gulf of Gökova in 227 BC, 199-198 BC, 142-144 AD, 1741, 1851, 1863, and 1869 [75]. The earthquake that caused the collapse of Bodrum was the 1493 earthquake [23]. Other historical records that occurred in the GofG are the earthquakes of 1741 (intensity: ?), 1851 (intensity: IX), 1863 (intensity: IX) and 1869 (intensity: VIII) [75].

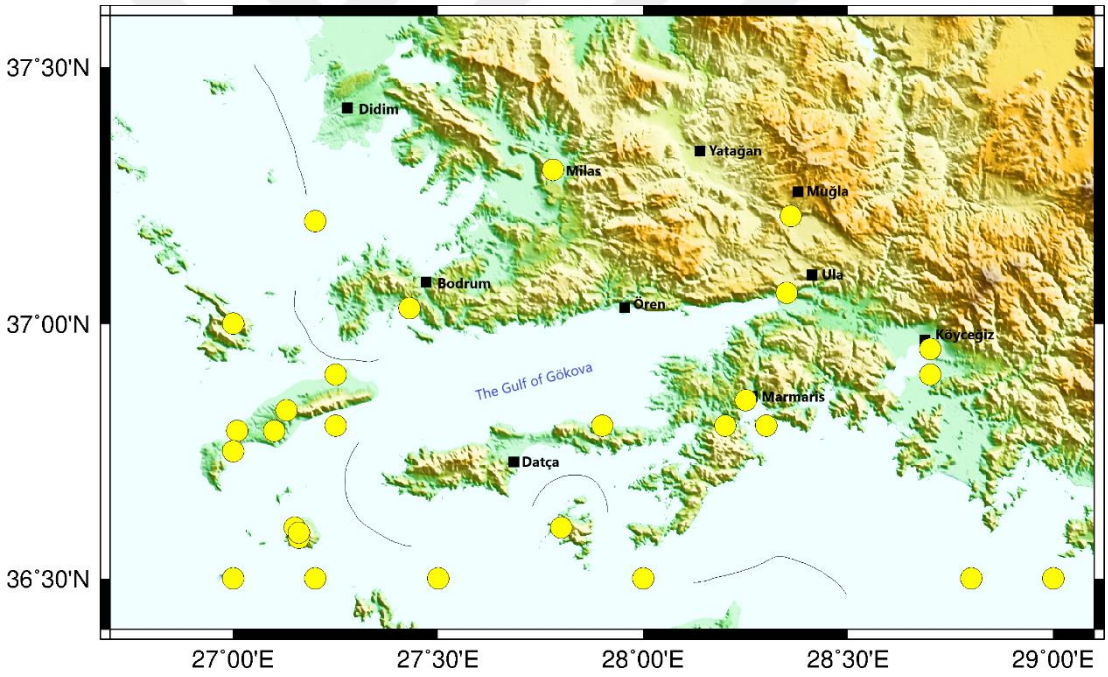


Figure 2.3: Distribution of historical period earthquakes in the GofG and its surroundings (Ambraseys, 2009) [75].

Table 2.1: The list of historical earthquakes of the region (AFAD).

| No | Date | Long. (°E) | Lat. (°N) | Location | Intensity |
|---|---|---|---|---|---|
| 1 | BC 5 | 36.83 | 27.13 | İstanköy (Kos) Island and Rodos | VIII |
| 2 | BC 24 | 36.50 | 27.00 | İstanköy (Kos) Island | VIII |
| 3 | BC 227 | 36.50 | 28.00 | Rodos | X |
| 4 | BC 412 | 36.50 | 27.00 | İstanköy (Kos) Island | VIII |
| 5 | AD 141 | 37.06 | 28.35 | the Gulf of Gökova | VIII |
| 6 | AD 335 | 36.79 | 27.01 | İstanköy (Kos) Island | ? |
| 7 | AD 465 | 36.79 | 27.01 | İstanköy (Kos) Island | VIII |
| 8 | AD 503 | 36.79 | 27.01 | İstanköy (Kos) Island, Datça | VIII |
| 9 | AD 1304 | 36.50 | 27.50 | Rodos Crete Cyprus-Hellenic Arc | X |
| 10 | AD 1422 | 36.60 | 27.15 | Nisiros Island Gulf of Kerme | ? |
| 11 | AD 1437 | 36.79 | 27.10 | İstanköy (Kos) Island | V |
| 12 | AD 1493 | 36.75 | 27.00 | İstanköy (Kos) Island | IX |
| 13 | AD 1495 | 37.00 | 27.00 | Kalimnos and Leros Islands | VI |
| 14 | AD 1571 | 36.79 | 27.10 | İstanköy (Kos) Island(Stanchio) | ? |
| 15 | AD 1673 | 36.79 | 27.10 | İstanköy (Kos) Island | ? |
| 16 | AD 1833 | 36.79 | 27.10 | Sakız Island-Aegean Sea | ? |
| 17 | AD 1843 | 36.90 | 27.25 | İstanköy (Kos) Island-Aegean Sea , Yunanistan(Khalki) | IX |
| 18 | AD 1851 | 37.21 | 28.36 | Muğla | ? |
| 19 | AD 1857 | 36.58 | 27.16 | Greece- Nisiros | ? |
| 20 | AD 1857 | 37.30 | 27.78 | Milas | VI |
| 21 | AD 1858 | 36.85 | 28.25 | Marmaris-Muğla | ? |
| 22 | AD 1862 | 36.80 | 28.30 | Marmaris and Rodos | VII |
| 23 | AD 1862 | 36.85 | 28.25 | Marmaris | VI |
| 24 | AD 1863 | 36.50 | 28.00 | İstanköy (Kos) Island, Hellenic Arc | IX |
| 25 | AD 1864 | 36.79 | 27.10 | İstanköy (Kos) | ? |
| 26 | AD 1869 | 36.60 | 27.80 | Sömbeki, Rodos and Kalimnos Islands | VIII |
| 27 | AD 1869 | 36.80 | 27.90 | the Gulf of Kerme, Marmaris, Muğla | VIII |
| 28 | AD 1870 | 36.50 | 28.80 | Makri-Greece | VII |
| 29 | AD 1870 | 36.50 | 29.00 | Fethiye and Rodos Island | VIII |
| 30 | AD 1871 | 36.80 | 28.20 | Marmaris and Sporat Islands | VII |
| 31 | AD 1873 | 36.50 | 27.20 | Nisiros Island-Aegean Sea | VII |
| 32 | AD 1873 | 36.59 | 27.16 | Nisiros Island-Aegean Sea | ? |
| 33 | AD 1873 | 36.59 | 27.16 | Nisiros Island-Aegean Sea | ? |
| 34 | AD 1885 | 37.20 | 27.20 | Messene, Kalamai-Greece | IX |
| 35 | AD 1887 | 36.90 | 28.70 | Köyceğiz, Muğla, Çine | VII |
| 36 | AD 1890 | 37.03 | 27.43 | Bodrum-Muğla | V |
| 37 | AD 1890 | 36.80 | 27.25 | İstanköy (Kos) Island-Aegean Sea | VII |
| 38 | AD 1891 | 36.79 | 27.10 | İstanköy (Kos) Island-Aegean Sea | ? |
| 39 | AD 1894 | 36.79 | 27.10 | İstanköy (Kos) Island-Aegean Sea | VI |
| 40 | AD 1896 | 36.50 | 28.00 | Rodos Island | VIII |
| 41 | AD 1896 | 37.21 | 28.36 | Muğla | VI |
| 42 | AD 1896 | 36.80 | 28.30 | Marmaris and its surroundings-Muğla | VII |
| 43 | AD 1897 | 36.80 | 28.30 | Marmaris, Ula, Köyceğiz, Fethiye and Rodos | VII |
| 44 | AD 1900 | 36.95 | 28.70 | Köyceğiz | ? |

### 2.2.2. Instrumental Seismicity and Analysis of the Seismicity

In order to explore instrumental period earthquakes from 1900 to the present, the earthquake catalog of the ISC (International Seismological Center) which compiles catalogs and phase data from earthquake research centers including KRDAE and AFAD, is examined. The epicenteral distributions of these earthquakes are generally aligned in a NE-SW direction and are shown in Figure 2.4. Clusters are also observed in places along this direction. It is observed that the seismic activity is more intense in the northern border of the GofG and the onshore areas in the inner regions compared to the southern regions. Some of the onshore clusters observed in the west of Muğla city center originate from coal and quarry mining activities in the region. Intense explosions in these areas can be recorded as earthquakes. In Figure 2.5, the 3D distribution of depth and magnitude of all earthquakes in the region are given.

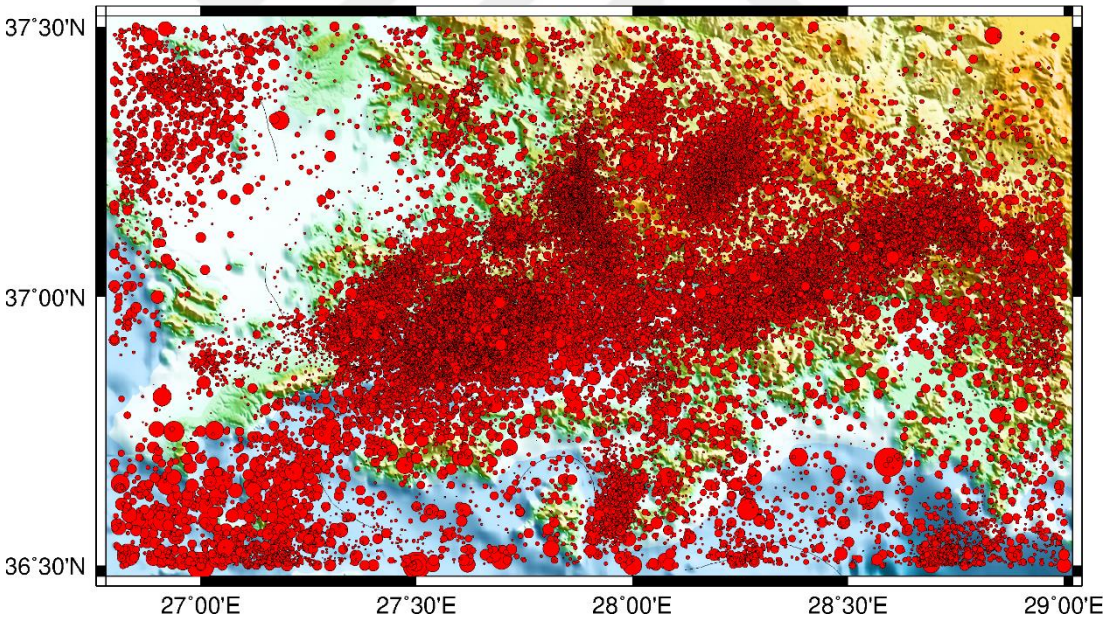


Figure 2.4: Distribution of earthquakes between years 2006-2022 in the GofG and its surroundings.

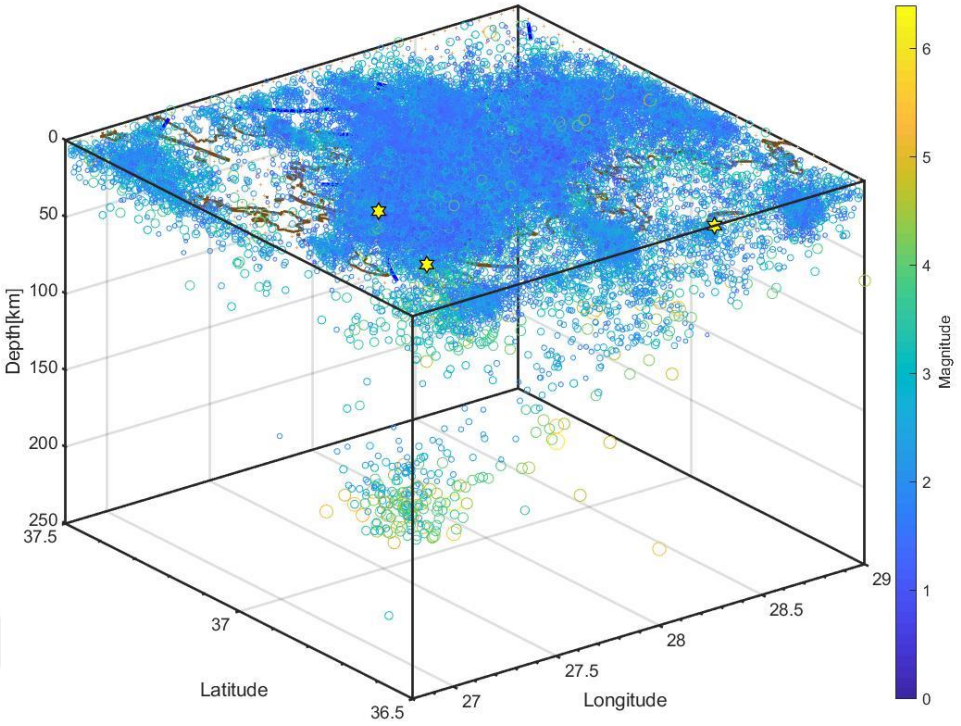


Figure 2.5: Depth and magnitude distribution of earthquakes in the GofG and its vicinity. Earthquakes marked with a yellow star represent the M>6.0 earthquakes in the area.

The total number of earthquakes recorded in the study area within years 2006-2022 is shown in Figure 2.6a and a close up 2013 to December 2022 is seen in the histogram 2.6b. The most striking observation here is the increase in the number of earthquakes around the Mw 6.3 2017 Bodrum-İstanköy (Kos) earthquake. Another notable issue in Figure 2.6b is the difference between the number of earthquakes that occurred prior to and following 2017 event. It can be observed that there has been a decline in the seismic activity in the region over the years after the Bodrum earthquake that occurred in July 2017.

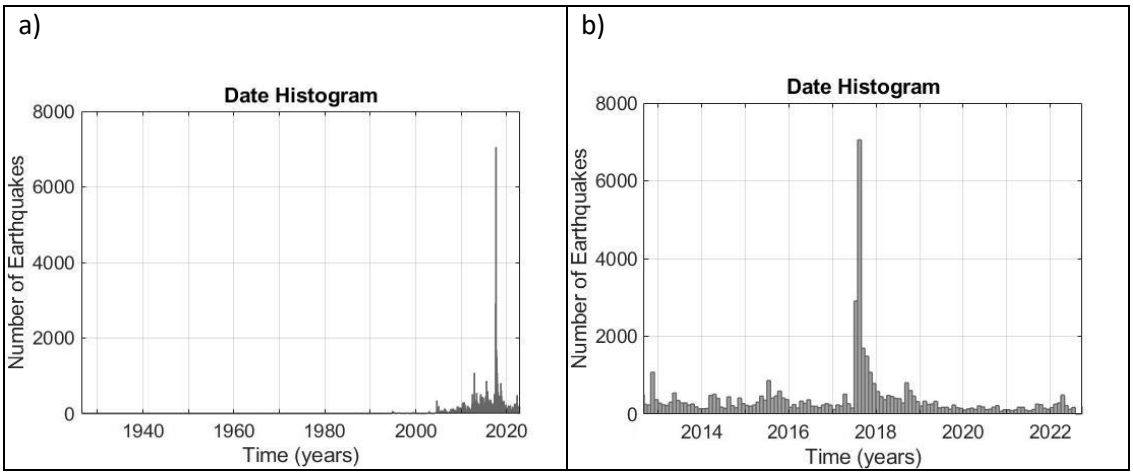


Figure 2.6: Annual numbers of earthquakes in the Gulf of Gökova and its surroundings a) from 1900 to the present and b) from 2013 to the present.

According to the ISC catalogue, the first earthquake record in the study area is on 05.07.1926. The number of earthquakes registered from this date until 01.12.2022 is 59,373. Earthquakes without magnitude information or depth information are excluded. 6,105 of the earthquakes were reported as 0 km. Reported earthquake depths range from 0.1 km to 203.6 km. The most reported earthquake depths are between 5-10 km (Figure 2.7.a). In Figure 2.7.b, it is observed that, since 1900, the largest number of earthquakes is 1.8.

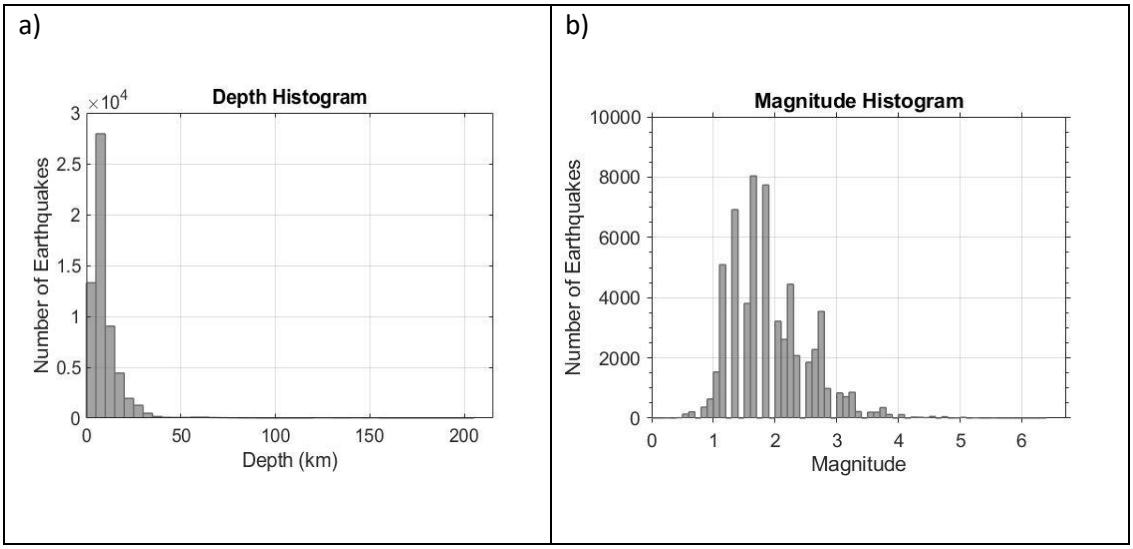


Figure 2.7: a) the depth and b) the magnitude distribution of all earthquakes that have occurred in the Gulf of Gökova and its surroundings since 1900.

The epicentral distributions of 52 earthquakes with magnitudes M ≥ 5.0 that occurred during the instrumental period in the area are shown in Figure 2.11. The epicenteral locations of these earthquakes are aligned along a NE-SW direction. Most of these earthquakes occured in the gulf with a few of them occurred onshore. The largest earthquake recorded in the region since 1900 is the 2017 Bodrum earthquake of with a magnitude of Mw 6.6 (Ms 6.3). The earthquake with a magnitude of 6.4 on 1961 occurred off the coast of Sarıgerme, and the third largest earthquake (Ms 6.3) occurred on the south of İstanköy (Kos) Island on 23.04.1933. The graph of cumulative moment release through years shown in Figure 2.8. The sharp increase of cumulative moment release can explain the occurrence of mainshocks. For this data, graphs of magnitude change in time and cumulative number of earthquakes in years are plotted. According to Figure 2.9 only the earthquakes with M > 4.0 were recorded until the late 1960s. In the late 2000s, the dataset became denser with the addition of earthquake records with smaller magnitudes. According to Figure 2.10, the number of recorded earthquakes increased in the mid-90s and changed dramatically in the mid-2000s.

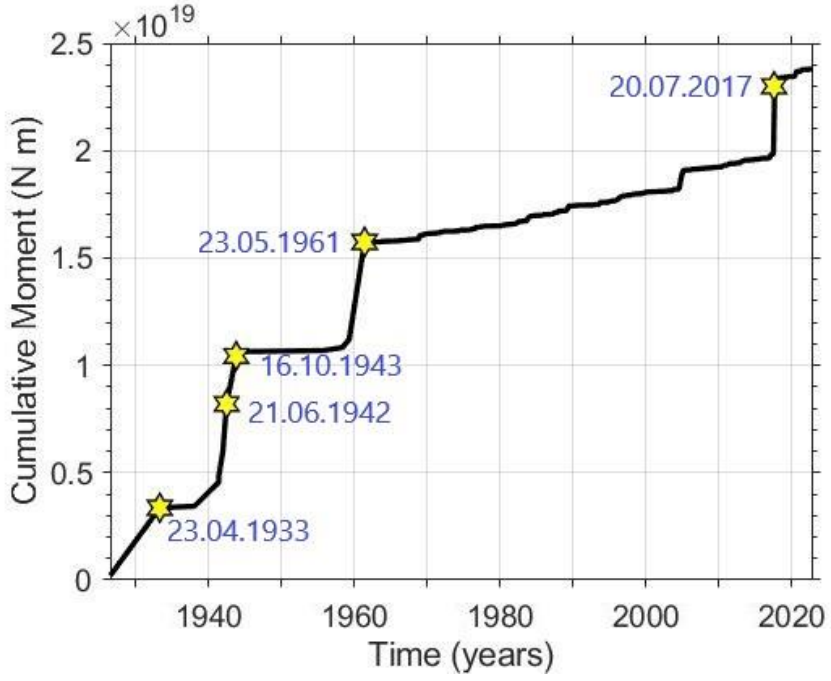


Figure 2.8: Cumulative moment release in years.

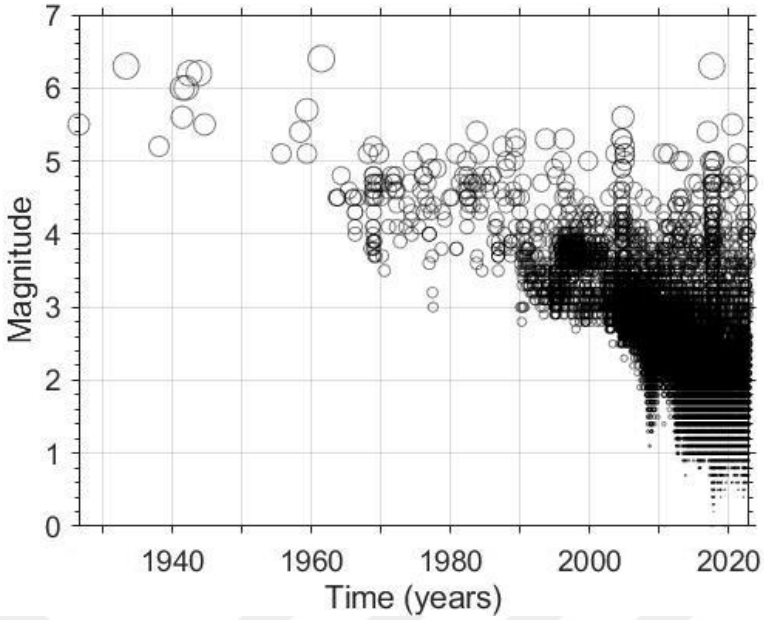


Figure 2.9: Magnitude vs time in years.

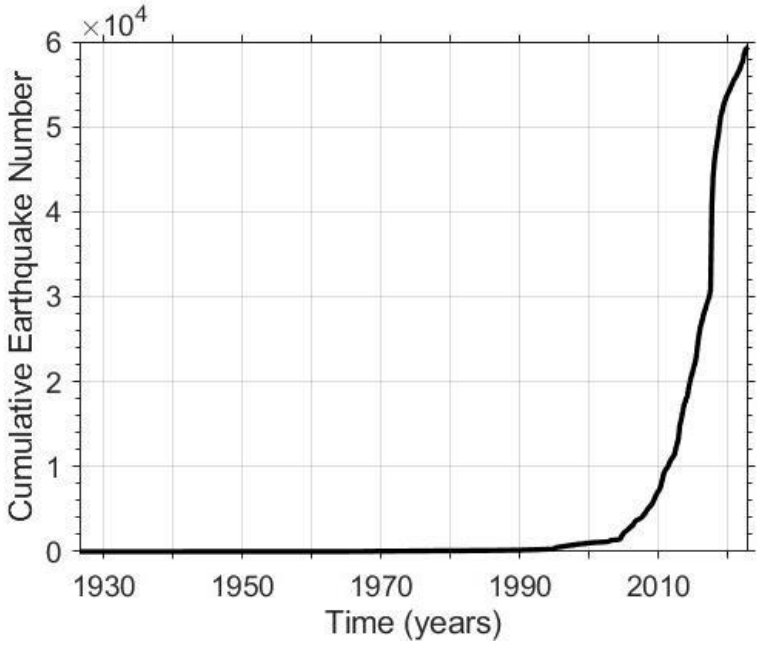


Figure 2.10: Cumulative number of earthquakes vs time in years.

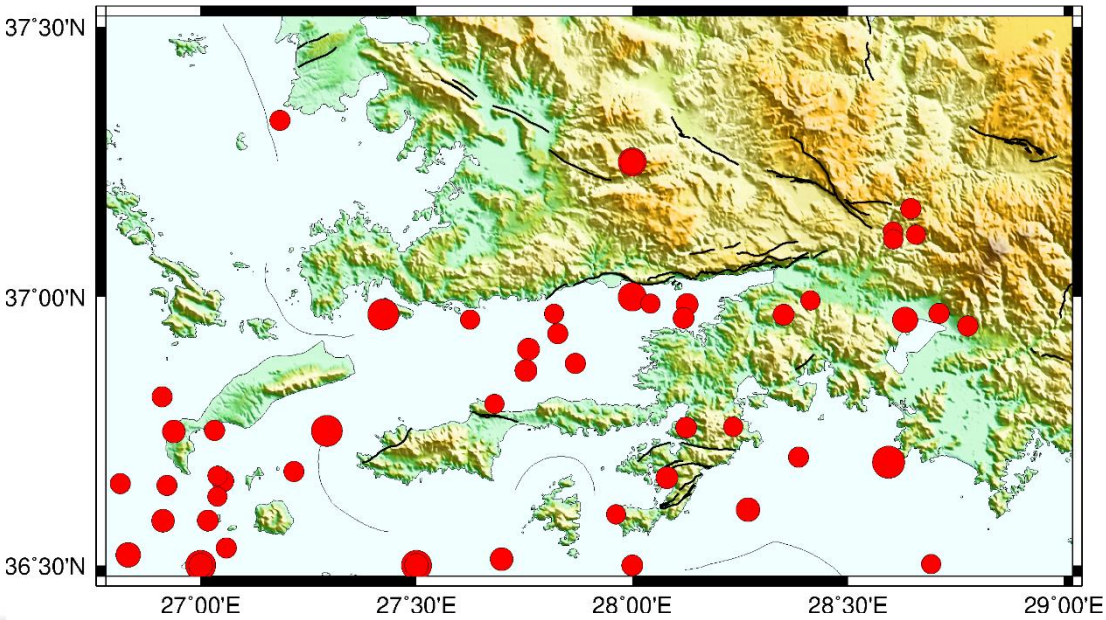


Figure 2.11: Epicentral distributions of the earthquakes (red filled circles) with magnitude M ≥ 5.0 that occurred in the GofG and its surroundings.

# 3. REGIONAL MOMENT TENSOR INVERSION ANALYSIS

In the first part of this study, in order to reveal the geometry of an earthquake and the related faulting mechanism, focal mechanisms are calculated. Seismic records are used to obtain focal mechanism "beachball" that provides information on the earthquake parameters, such as epicenter, depth, size, strike, slip and rake of the fault which are illustrated in Figure 3.1 [76]. The fault plane, with normal vector $\hat{n}$, divides the footwall block from the hanging wall block. The slip vector, $\hat{d}$, describes how the hanging wall block moves in relation to the footwall block. The $x_3$ axis is vertical and $x_1$ is oriented along the fault in the plane of the Earth's surface, such that the fault dip angle, $\delta$, measured from the $-x_2$ axis, is less than 90°. The slip angle $\lambda$ is measured in the fault plane between the $x_1$ and $x_2$ axes. The strike of the fault, $\phi$, measured clockwise from north.

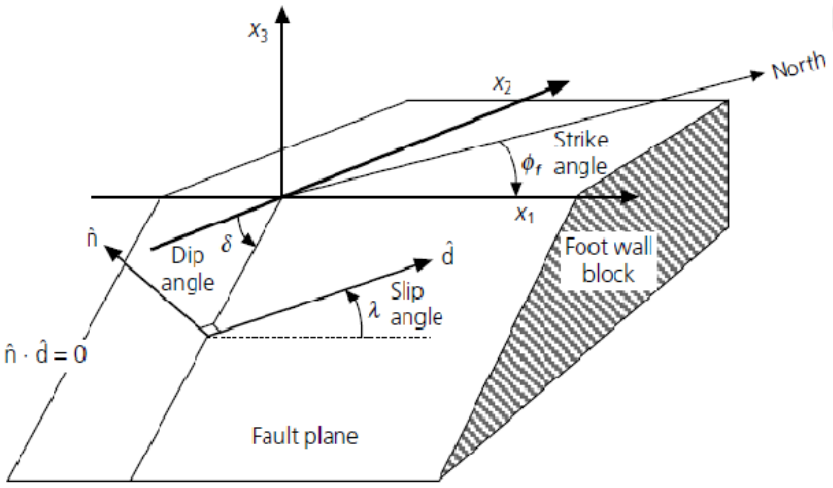


Figure 3.1: The demonstration of fault geometry [76].

There are several methods in literature for estimating focal mechanisms, such as utilizing first motion polarity of body waves (P and S), waveform modeling and moment tensor inversion. Exploiting the seismic moment tensor (MT) is to investigate the source parameters (strike, dip, and rake or slip) and the scalar seismic moment (and thus the moment magnitude) is a straightforward technique.

## 3.1. Theoretical Background

The seismic moment tensor (MT) is a mathematical representation of the seismic source revealing the rupture process and fault source parameters through inversion modeling. The most important aspect of the MT is that it provides a complete specification of the equivalent forces of a seismic point source. Figure 3.2 depicts all of the equivalent forces of a single force, a single couple force, and a double couple forces. Seismic waves are produced when energy is suddenly released through the Earth. Rapid release is essential to trigger propagating seismic waves; otherwise, alternative methods are used to record gradual deformation in the crust [76]. According to the single-couple concept, earthquakes happen as a result of a fault slipping, and this slipping is related to a single couple, which includes two forces moving in opposite directions along the fault [77].

The double couple (DC) is an efficient technique for simulating the pattern of radiated energy at the earthquake source. This model is built around two force couples that have equal moments in opposite directions. These force pairs are perpendicular to each other, so there is no net moment [77]. Double couple assumes that there is only one direction of motion along a fault during slip. According to their various combinations, in Figure 3.3 the double couple of equivalent forces are shown. A seismic MT is used to describe the equivalent forces of a seismic point-source [78]. The fault parameters such as strike, dip, rake and the seismic moment can be calculated using the seismic MT.

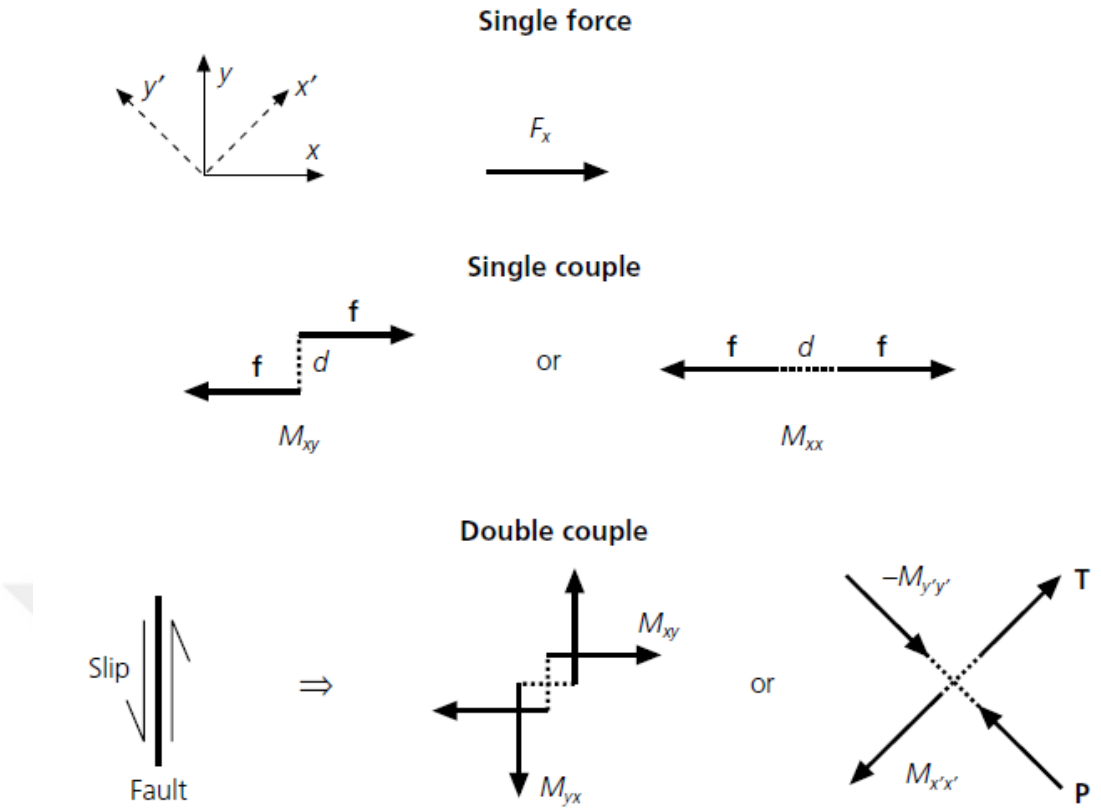


Figure 3.2: Demonstration of equivalent body forces. The two forms of force couples are $M_{xx}$, which is a force dipole with no applied torque, and $M_{xy}$, which is a force couples with torque. Slip on a fault can be characterized by the superposition of couples such as $M_{xy}$ and $M_{yx}$ or dipoles such as $M_{x'x'}$ and $M_{y'y'}$.

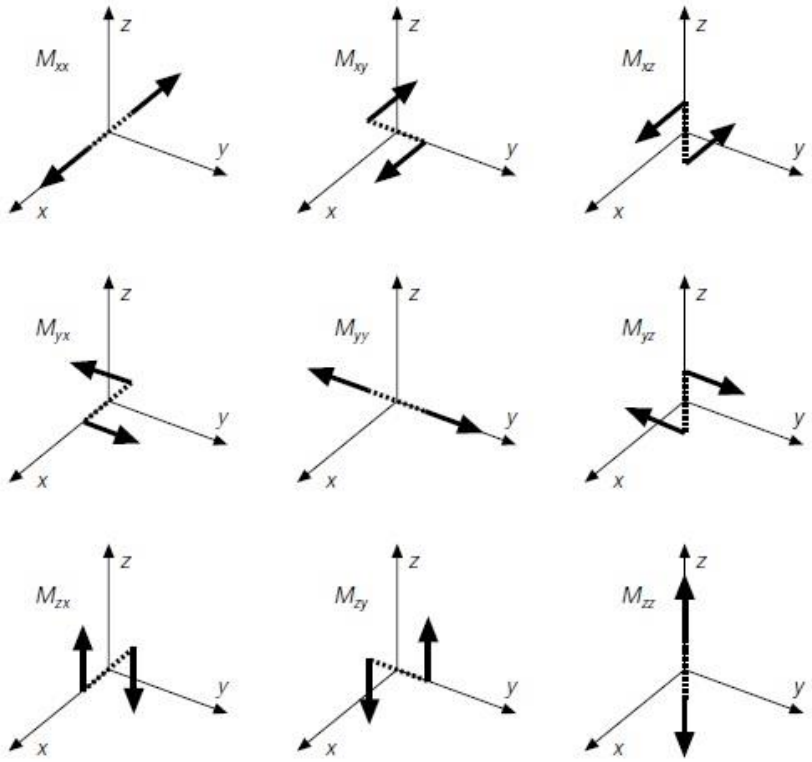


Figure 3.3: The demonstration of seismic moment tensor's nine force couples [77].

The earthquake's scalar seismic moment tensor ($M_o$) is the magnitude of force equivalents associated with the event's size and torque dimensions. The seismic moment tensor (**M**) is written as follows:

$$\mathbf{M} = \begin{bmatrix} M_{xx} & M_{xy} & M_{xz} \\ M_{yx} & M_{yy} & M_{yz} \\ M_{zx} & M_{zy} & M_{zz} \end{bmatrix} \tag{3.1}$$

The non-diagonal elements should be symmetric in accordance with the law of momentum conservation, leaving six independent pairs [77]. Diagonalizing the moment tensor matrix into an eigenvector system results in three forces: the tension (T) axis, the null (B) axis and the pressure (P) axis with eigenvalues $\lambda_T \geq \lambda_B \geq \lambda_P$. The compressional and dilatational quadrants are represented by the P and T axes, respectively [79].

The components of the seismic moment tensor for a double-couple earthquake are given by the scalar seismic moment ($M_o$), as well as the elements of the unit fault normal vector ($\hat{n}$) and the unit slip vector ($\hat{d}$).

$$M_{ij} = M_0 \begin{bmatrix} 2n_x d_x & n_x d_y + n_y d_x & n_x d_z + n_z d_x \\ n_y d_x + n_x d_y & 2n_y d_y & n_y d_z + n_z d_y \\ n_z d_x + n_x d_z & n_z d_y + n_y d_z & 2n_z d_z \end{bmatrix} \quad (3.2)$$

This demonstrates that the moment tensor is symmetrical, i.e.

$$M_{xy} = M_{yx}, M_{xz} = M_{zx}, M_{yz} = M_{zy} \quad (3.3)$$

This suggests that slip on the fault plane or on the auxiliary plane produces the same seismic radiation pattern. It is also clear that the trace (the total of the diagonal elements) is equal to zero. A non-zero trace would imply a change in volume (e.g., an explosion), which would not be present in the case of a pure double-couple source [76].

The MT can be expressed in terms of the seismic moment, and the fault components using equations that represent the fault normal and slip vectors in terms of rake ($\lambda$), dip ($\delta$) and strike ($\phi$):

$$\hat{n} = \begin{bmatrix} -sin\delta sin\phi \\ -sin\delta cos\phi \\ cos\delta \end{bmatrix} \quad (3.4)$$

$$\hat{d} = \begin{bmatrix} cos\lambda cos\phi + sin\lambda cos\delta sin\phi \\ -cos\lambda sin\phi + sin\lambda cos\delta cos\phi \\ sin\boldsymbol{\lambda} sin\delta \end{bmatrix} \quad (3.5)$$

Utilizing the definition of the seismic MT which depends on the fault normal and slip vectors together with equations 3.4 and 3.5, relations for each of the moment tensor elements with respect to strike, rake and dip can be derived. There are only six elements to be derived because Equation 3.1 is symmetric.

$$
\begin{aligned}
M_{xx} &= -M_0\,(sin\delta sin2\phi cos\lambda + sin2\delta sin^2\phi sin\lambda) \\
M_{xy} = M_{yx} &= -M_0\,(sin\delta sin2\phi cos\lambda + 1/2\, sin2\delta sin2\phi sin\lambda) \\
M_{xz} = M_{zx} &= M_0\,(cos2\delta sin\phi sin\lambda + cos\delta cos\phi cos\lambda) \\
M_{yy} &= -M_0\,(sin\delta sin2\phi cos\lambda - sin2\delta cos^2\phi sin\lambda) \\
M_{yz} = M_{zy} &= -M_0\,(cos\delta sin\phi cos\lambda - cos2\delta cos\phi sin\lambda) \\
M_{zz} &= M_0\,(sin2\phi sin\lambda)
\end{aligned}
\tag{3.6}
$$

Information on the equivalent forces of the moment tensor can be obtained from the analysis of eigenvalues and eigenvectors. The volume change of the source is represented by the sum of the eigenvalues. If the sum of the eigenvalues is M > 0, then the moment tensor is isotropic and relates to a volume change. If the sum of the eigenvalues M = 0, then the moment tensor can only be resolved into deviatoric components; major and minor double couples; or a double couple (DC) and a compensated linear vector dipole (CLVD) [78].

$$
M_{dev} = \begin{bmatrix} \lambda_1 & 0 & 0 \\ 0 & \lambda_2 & 0 \\ 0 & 0 & \lambda_3 \end{bmatrix}; |\lambda_1| \geq |\lambda_2| \geq |\lambda_3| \tag{3.7}
$$

$$
M_{dev} = \begin{bmatrix} \lambda_1 & 0 & 0 \\ 0 & -\lambda_1 & 0 \\ 0 & 0 & 0 \end{bmatrix} + \begin{bmatrix} 0 & 0 & 0 \\ 0 & -\lambda_3 & 0 \\ 0 & 0 & \lambda_3 \end{bmatrix} \tag{3.8}
$$

$$
M_{dev} = \begin{bmatrix} \frac{2\lambda_1 + \lambda_3}{2} & 0 & 0 \\ 0 & -\frac{2\lambda_1 + \lambda_3}{2} & 0 \\ 0 & 0 & 0 \end{bmatrix} + \begin{bmatrix} \frac{-\lambda_3}{2} & 0 & 0 \\ 0 & \frac{-\lambda_3}{2} & 0 \\ 0 & 0 & \lambda_3 \end{bmatrix} \tag{3.9}
$$

Equation 3.8 represents the moment tensor as major and minor double couples whereas, equation 3.9 represents double couple and compensated linear vector dipole components of a moment tensor. CLVD mechanisms can be triggered by cracks emerging under tension or by two earthquakes occurring at roughly the same time and location on faults with distinct geometries [76].

In Figure 3.4 expected moment tensors and their associated focal mechanisms can be seen. The isotropic MT is shown in the first row (an explosion is represented on the left and an implosion is represented on the right). The next three rows are examples of pure double-couple mechanisms. The second row demonstrates strike-slip faulting. The third row is characterized by vertical dip-slip faulting. The fourth

row represents pure reverse faulting. Finally, CLVD sources are represented by the last two lines [76].

| Moment tensor | Beachball | Moment tensor | Beachball |
|---|---|---|---|
| $\frac{1}{\sqrt{3}}\begin{pmatrix}1&0&0\\0&1&0\\0&0&1\end{pmatrix}$ |  | $-\frac{1}{\sqrt{3}}\begin{pmatrix}1&0&0\\0&1&0\\0&0&1\end{pmatrix}$ | 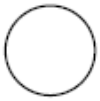 |
| $-\frac{1}{\sqrt{2}}\begin{pmatrix}0&1&0\\1&0&0\\0&0&0\end{pmatrix}$ |  | $\frac{1}{\sqrt{2}}\begin{pmatrix}1&0&0\\0&-1&0\\0&0&0\end{pmatrix}$ |  |
| $\frac{1}{\sqrt{2}}\begin{pmatrix}0&0&-1\\0&0&0\\-1&0&0\end{pmatrix}$ |  | $\frac{1}{\sqrt{2}}\begin{pmatrix}0&0&0\\0&0&-1\\0&-1&0\end{pmatrix}$ |  |
| $\frac{1}{\sqrt{2}}\begin{pmatrix}-1&0&0\\0&0&0\\0&0&1\end{pmatrix}$ |  | $\frac{1}{\sqrt{2}}\begin{pmatrix}0&0&0\\0&-1&0\\0&0&1\end{pmatrix}$ |  |
| $\frac{1}{\sqrt{6}}\begin{pmatrix}1&0&0\\0&-2&0\\0&0&1\end{pmatrix}$ |  | $\frac{1}{\sqrt{6}}\begin{pmatrix}-2&0&0\\0&1&0\\0&0&1\end{pmatrix}$ |  |
| $\frac{1}{\sqrt{6}}\begin{pmatrix}1&0&0\\0&1&0\\0&0&-2\end{pmatrix}$ |  | $-\frac{1}{\sqrt{6}}\begin{pmatrix}1&0&0\\0&1&0\\0&0&-2\end{pmatrix}$ |  |

Figure 3.4: Moment tensor examples and focal mechanism steroplots.

### 3.1.1. Focal Mechanism

In this study, we firstly calculated the earthquake focal mechanisms (FM) to explore the source characteristics of earthquakes occurred in the GofG, Earthquake FM solutions enable researchers to gain crucial knowledge on the stress of the Earth's crust. Seismograms record ground motions (seismic waves) in order to build up focal mechanism graphs that providing details of earthquakes, such as epicenter, origin time, depth, size, strike, slip and rake of the fault. [76]. There are several methods in the literature for estimating FM, such as first motion polarity of body waves (P and S), waveform modeling and moment tensor inversion.

The characteristics of the movement at the earthquake hypocenter can be determined from the initial movements of the P waves. Some of the first motions of P wave are from the earthquake hypocenter to the seismic station, and some are from the station to the hypocenter. If the direction of the first motion is toward the focus, it is in the dilatation zone, and if it is outward from the focus, it is in the compression zone. The quadrants consist of two compression zones and two dilatation zones which are divided by the fault plane and the auxiliary plane. Orientation of these planes defines the characteristics of the fault. Figure 3.5 demonstrates two nodal planes of a fault separate the compressional and the dilatational regions of an earthquake's first arrivals.

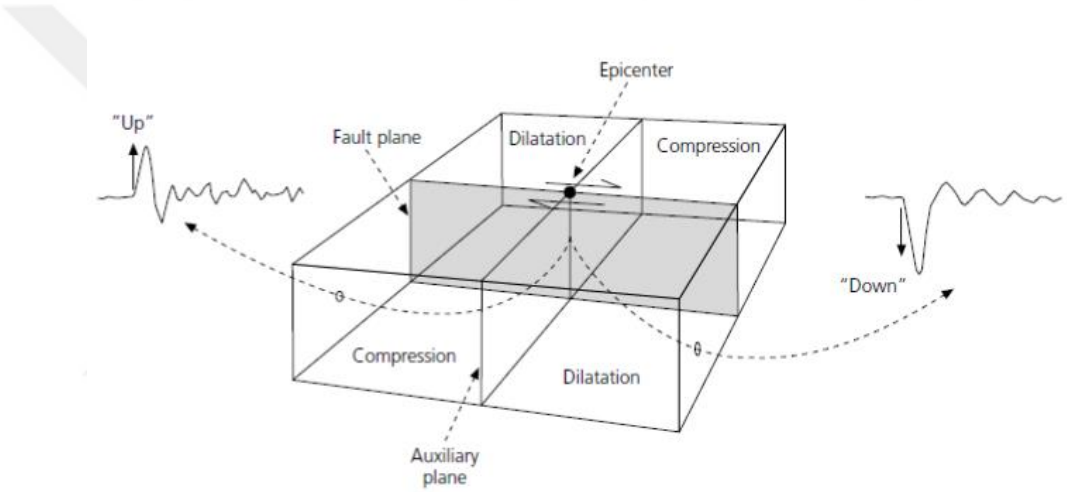


Figure 3.5: Demonstration of dilatational and compressional regions of a fault [76].

Waveform modeling, on the other hand, compares observed body waves and surface waves with synthetic waveforms to find the best fitting model for the data. Rather than using the first motion polarity method, waveform modeling can be used to determine the depth of earthquakes and the rupture processes. Synthetic waveforms are generated information on ground structure, earthquake source, and seismometer features, as shown below:

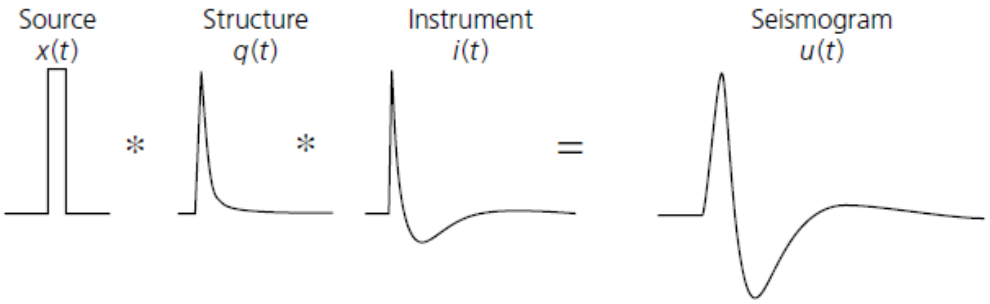


Figure 3.6: Components of a waveform

In Figure 3.6 x(t) represents the source time function of the signals diffused through the ground, q(t) represents the effects of the earth's structure through which the waves are traveling, i(t) is the seismometer's instrument response to ground motion for various frequencies [76].

The source signals, commonly referred to as the body wave signals generated by an earthquake rupture, can be expressed as a source time function. Instead of impulses, faults produce complex source time functions since each point doesn't break simultaneously. For simplification, it is assumed that the earthquake is a single point source and is represented by a ramp function that depicts the fault's displacement as a ramp. In the ramp function, the slip begins at time zero and stops at the beginning of the rising point. Therefore, the length of the fault is calculated as the total number of seismic point sources multiplied by their rise and rupture times [76].

## 3.2. Moment Tensor Inversion Method

The moment tensor (MT) contains information about the force couples and is a representation of the source of the earthquake [76]. Seismic moment tensors provide important characteristics of earthquakes, such as moment magnitude, origin time, source location, fault type and tectonic regime, therefore reliable moment tensor inversion is crucial in the study of source parameters. The MT inversion allows the calculation of faulting source parameters from observed seismic recordings.

In seismology, inversion processes are classified as global, regional, and local with respect to dimension. In this study, the centroid moment tensor (CMT) is

calculated at a regional scale. In CMT inversion, six independent components of the moment tensor and the source point coordinates are estimated together. The CMT inversion is a linear least squares operation.

The MT inversion analysis is carried out by Computer Programs in Seismology 3.30, which uses full-waveform seismograms to assess the correlation between observed and synthetic waveforms in order to calculate the moment tensor [80].

Elastic displacement at any station caused by an earthquake can be explained as the convolution of time dependent moment tensor components and time dependent green functions, using the point-source assumption.

$$u_s(x,t) = M_{kj}(\xi,t) * G_{skj}(x,\xi,t) \tag{3.10}$$

Here, $u_s(x,t)$ is the displacement at point x; $M_{kj}(\xi,t)$ quadratic symmetric seismic MT components; $G_{skj}(x,\xi,t)$ Green functions corresponding to the source coordinates, where x: $x_1$=north, $x_2$=east, x3=position vector for the corresponding station and; $\xi$ : $\xi_1$=north, $\xi_2$=east, $\xi_3$=down is the position vector for the point source. Here, *t* is time and *s* denote the component of the displacement.

The source time function, S(t), is the earthquake source signal produced by faulting. The seismogram can be written in terms of the observed waveform moment tensor components, Green function, and source time function S(t) as follows:

$$u_s(\mathbf{x},t) = \sum_{j=1}^{6} M_{kj}(\xi,t)\left[G_{skj}(\mathbf{x},\xi,t) * S(t)\right], \quad k = 1,2,3,\dots,6 \tag{3.11}$$

If the source time function S(t) is a unit function, the equation can be written as follows:

$$u_s(\mathbf{x},t) = \sum_{j=1}^{6} M_j(\xi) G_{skj}(t) \tag{3.12}$$

In the case of n number of seismogram recordings, the equation (3.12) can be expressed as a matrix and rewritten as follows:

$$\begin{bmatrix} u_1 \\ u_2 \\ \vdots \\ u_n \end{bmatrix} = \begin{bmatrix} G_{11} & G_{12} & \cdots & G_{16} \\ G_{21} & G_{21} & \cdots & G_{26} \\ \vdots & \vdots & \ddots & \vdots \\ G_{n1} & G_{n2} & \cdots & G_{n6} \end{bmatrix} . \begin{bmatrix} M_1 \\ M_2 \\ \vdots \\ M_6 \end{bmatrix} \quad (3.13)$$

Equation (3.13) can be written more generally as follows:

$$u = Gm \quad (3.14)$$

Since this system of equations has n equations and 6 unknowns (m), it is an over-defined system of linear equations. Since the matrix G is not square, it cannot be inverted. To solve this system, generalized inversion as in (3.15) should be used.

$$\mathrm{m} = \left(\mathrm{G}^{\mathrm{T}}\mathrm{G}\right)^{-1}\mathrm{G}^{\mathrm{T}}\mathrm{u} \quad (3.15)$$

### 3.2.1. Data

In this study, focal mechanism solutions of 140 earthquakes which have not been published elsewhere with a magnitude of M≥3.0 during the period January 2006 to December 2022 are calculated. Hence, we aim to fill a gap in the focal mechanism catalogue of the region to be further used in future studies. As stated in Chapter 2, the region is seismically active. The earliest date of the events included in this study is 2006 since the national seismic networks do not provide any digital data for an earlier date. The information on the hypocentral location and magnitude are obtained from KOERI catalogue. In addition to the earthquake data, XML files containing instrumental information were obtained from the relevant databases. Instrumental information includes both some parameters of the station (location, altitude, component information, sampling interval, etc.), as well as the response functions of seismometers (RESP and/or Pole-Zero information).

We calculated focal mechanisms of the earthquakes occurred in and around the GofG. Waveform data were obtained from national networks of NOA (Institute of Geodynamics-National Observatory of Athens), AFAD and KOERI. Hermann et al. (2013) algorithm based on the time domain moment tensor inversion technique was used for focal mechanism solutions in which the earthquake focal depth, moment

magnitude, strike, dip, and rake angles were determined [80]. A general crustal model is used to calculate the source parameters of regional earthquakes (Table 3.1). In addition to the these, the density and seismic attenuation factors (quality factor) of the same layer are also included.

Table 3.1: Crust model used to calculate green functions [80].

| *h (km)* | *Vp (km/s)* | *Vs (km/s)* | *P (g/cm$^3$)* | *Qp* | *Qs* |
|---|---|---|---|---|---|
| 1.9 | 3.4065 | 2.0089 | 2.2150 | 0.302E-02 | 0.679E-02 |
| 6.1 | 5.5445 | 3.2963 | 2.6089 | 0.349E-02 | 0.784E-02 |
| 13.0 | 6.2708 | 3.7396 | 2.7812 | 0.212E-02 | 0.476E-02 |
| 19.0 | 6.4075 | 3.7680 | 2.8223 | 0.111E-02 | 0.249E-02 |
| 0.0 | 7.9000 | 4.6200 | 3.2760 | 0.164E-10 | 0.370E-10 |

To generate a uniform database, data were trimmed into equal time slots; 10 s before the first arrival time of the P-phase to 120 s after. At this stage, the instrumental effect is also removed from the observational data. The velocity recordings are then converted to displacements. Before starting the inversion process, a three-pole Butterworth filter with a band range of 0.02-0.12 Hz is applied to the recordings. Additionally, a filter that removes the microseismic events is used to increase the signal-to-noise ratio, if needed. Stations with low signal quality, data with low S/N ratio and stations with an epicentral distance of more than 700 km are ignored. The main purpose of the moment tensor inversion method is to match the calculated synthetic seismograms with the observed waveforms recorded at the stations at regional distances. For this purpose, Green functions are calculated as described in Herrmann et al. [2013].

### 3.2.2. Results

The main purpose of the MT inversion method is to match the calculated synthetic seismograms with the observed waveforms recorded at the stations at regional distances. To do this, green functions are calculated as suggested in Herrmann et al. [2013]. In order to prepare the data for the inversion operations and to bring the data into equal time slots, both the observed and green functions are cut at an interval from 10 s before the first arrival time of the P-phase to 120 s after. At this stage, the instrumental effect is also removed from the observational data. The

velocity records are then converted to displacements. Before starting the inversion process, a three-pole Butterworth filter with a band range of 0.02-0.12 Hz is applied to the recordings. Additionally, a filter that removes the microseismic events is used to increase the signal-to-noise ratio, if needed. Stations with low signal quality, noise-containing data and stations with an epicentral distance of more than 700 km are ignored.

After the MT inversion processes, the parameters of the calculated focal mechanism solutions of 140 earthquakes that occurred in the region between 2006-2022 are given in Table 3.2 and demonstrated in Figure 3.7. It can be seen that the majority of earthquakes have a normal faulting regime and are aligned counterclockwise in the E-W direction. Another feature that stands out at first glance is the solutions clustered around Bodrum, Çökertme and Ula.

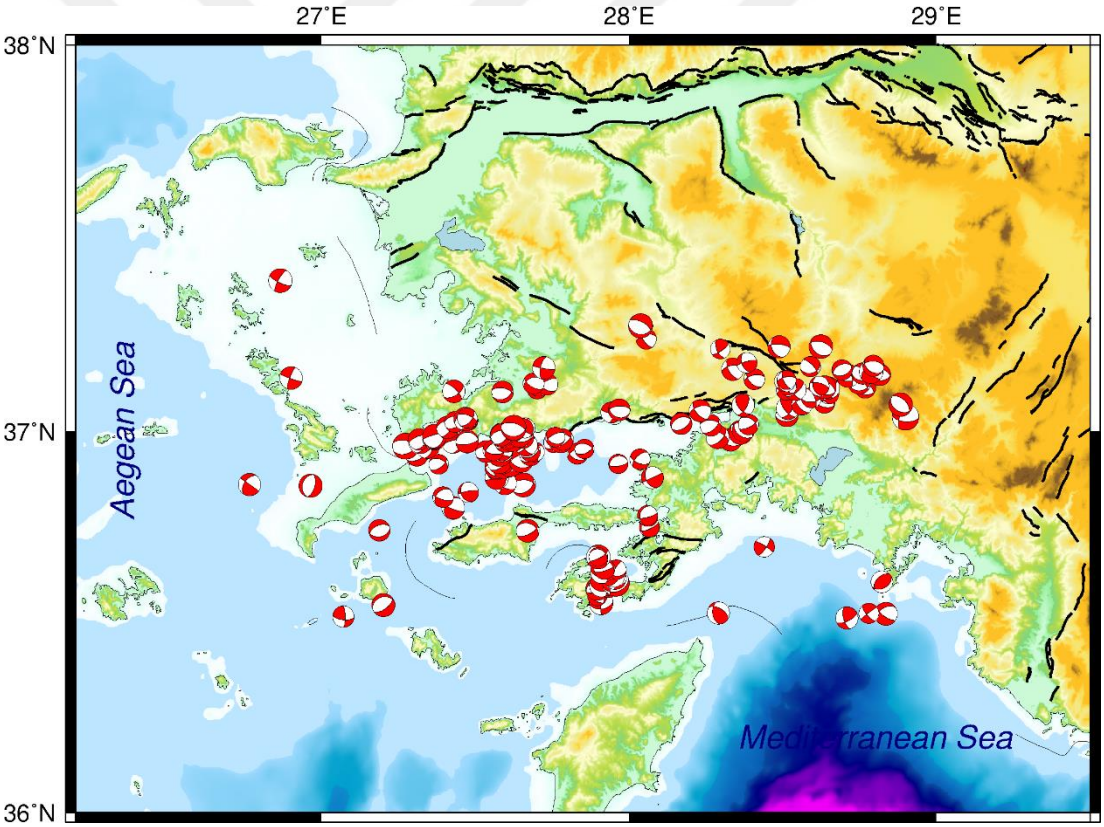


Figure 3.7: Focal mechanism solutions of 140 earthquakes.

The result of the FM solutions obtained by the moment tensor inversion method of the earthquake (Mw=4) that occurred on 21.07.2017 at 01:25:34 (GMT) is given in Figure 3.8. The earthquake's focal mechanism solution was completed using

waveform data provided by EIDA and TDVMS. The hypocentral parameters (origin time, location and depth) and the local magnitude were determined by KOERI. Stations with waveforms obtained by broadband velocity seismometers were used for FM solutions. Waveforms with a low signal-to-noise ratio were eliminated from the dataset. A bandpass filter in the range 0.06-0.08 Hz is used to the pre-inversion of the time signals. The location of seismic stations used for FMS is depicted in Fig. 3.8a. The goodness of fit to source depth is given in Figure 3.8b. The best FMS for the current event was obtained from a depth of 14 km. In addition, Fig. 3.8c shows a comparison of the observed (red) and predicted (blue) waveforms. The peak amplitudes of each observed-predicted component are shown by the numbers to the left of each trace. At the right of each estimated trace, a pair of numbers is shown in black. The lower number represents the percentage of variance reduction used to characterize the individual goodness of fit (a value of 100% implies a perfect fit). As a result of the inversion process of this earthquake, it has a high goodness of fit value of 76%.

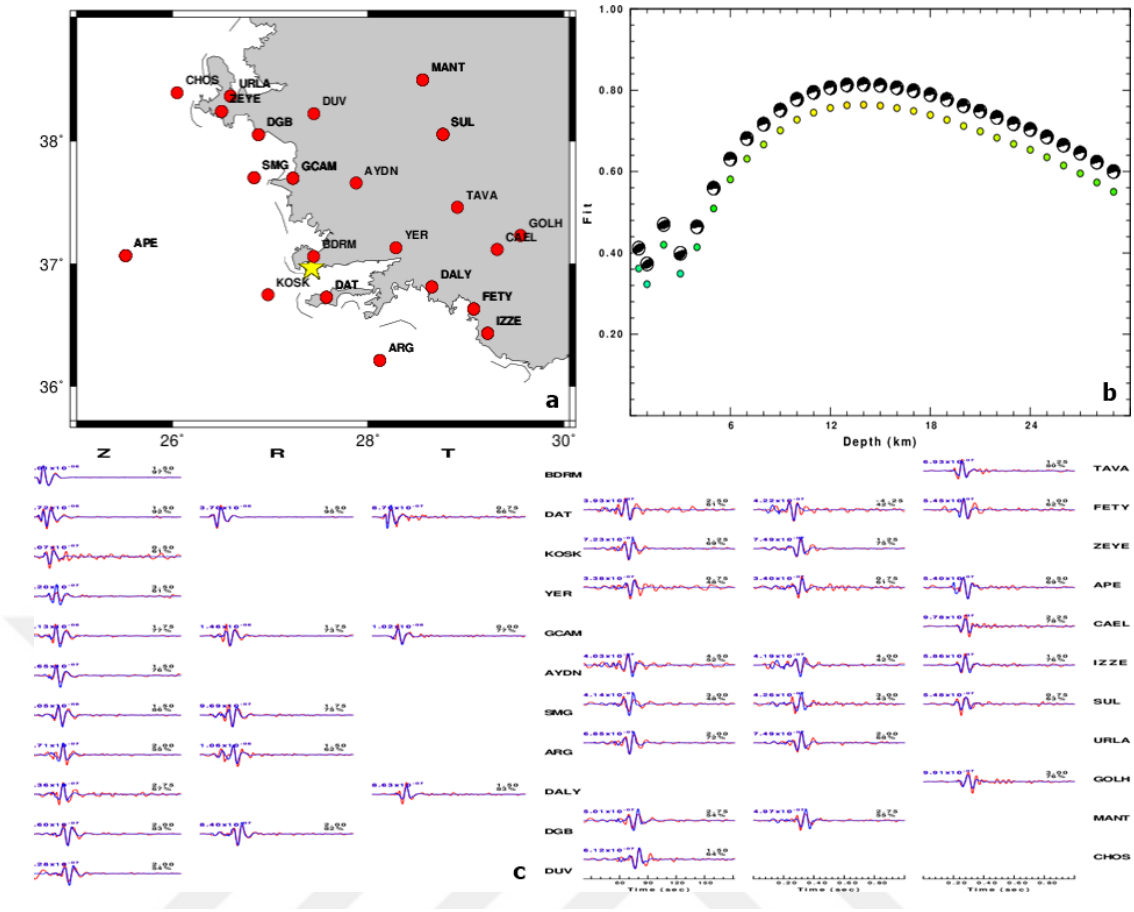


Figure 3.8: The results obtained by moment tensor inversion of the earthquake dated 21.07.2017. a) the stations where earthquake location and data are used, b) solution goodness of fit graph as a function of depth, c) representation of the observed (red) and artificial (blue) seismograms at each selected station and at each component (Z, R, T). Components that are not used due to noisy or poor recording are left blank.

The result of the focal mechanism solutions obtained by the moment tensor inversion method of the earthquake (Mw=3.48) that occurred on 17.01.2018 at 22:06:38 (GMT) is given in Figure 3.9. The earthquake's focal mechanism solution (FMS) was completed using waveform data provided by EIDA and TDVMS. The hypocentral parameters (origin time, location and depth) and the local magnitude were determined by KOERI. Stations with waveforms obtained by broadband velocity seismometers were used for FMS. Waveforms with a low signal-to-noise ratio were eliminated from the dataset. A bandpass filter in the range 0.06-0.08 Hz is used to the pre-inversion of the time signals. The location of seismic stations used for FMS is depicted in Fig. 3.9a. The goodness of fit to source depth is given in Figure 3.9b. The best FMS for the current event was obtained from a depth of 7 km. In

addition, Fig. 3.6c shows a comparison of the observed (red) and predicted (blue) waveforms. The peak amplitudes of each observed-predicted component are shown by the numbers to the left of each trace. At the right of each estimated trace, a pair of numbers is shown in black. The lower number represents the percentage of variance reduction used to characterize the individual goodness of fit (a value of 100% implies a perfect fit). As a result of the inversion process of this earthquake, it has a low goodness of fit value of 47%.

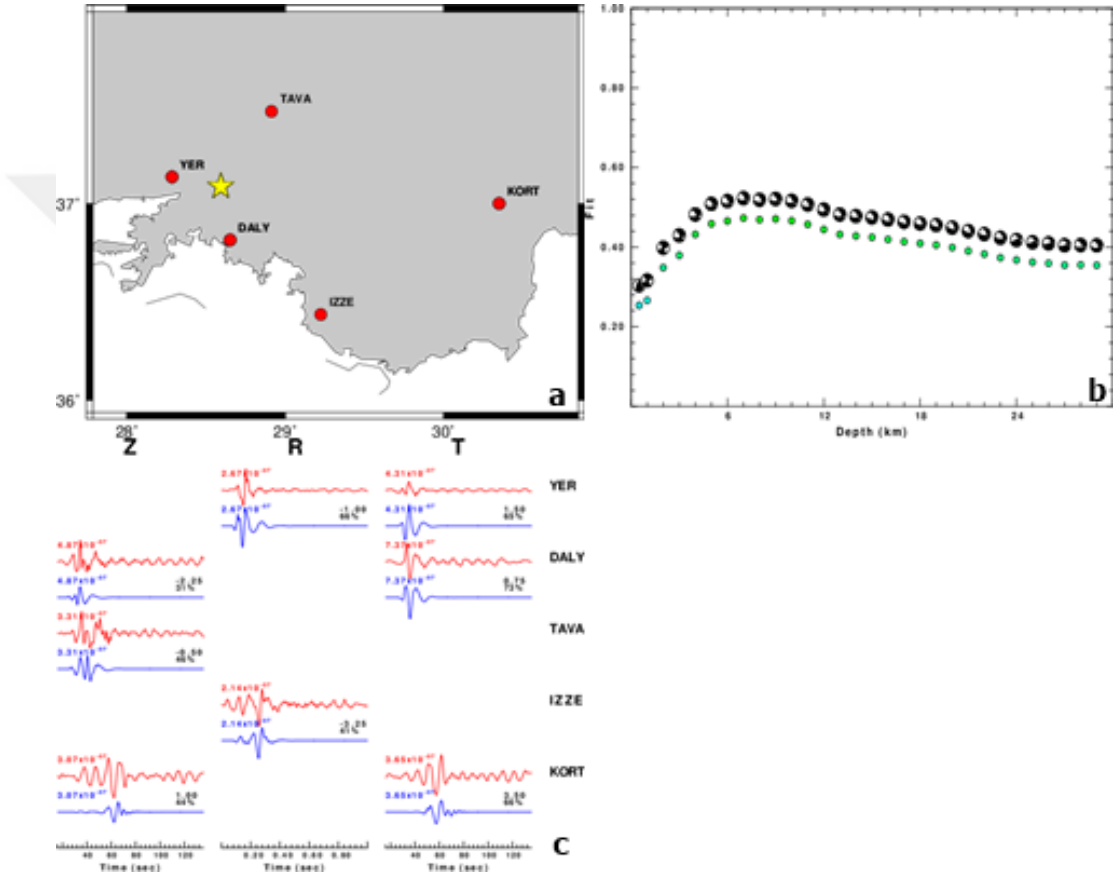


Figure 3.9: The results obtained by moment tensor inversion of the earthquake dated 17.01.2017. a) the stations where earthquake location and data are used, b) solution goodness of fit graph as a function of depth, c) representation of the observed (red) and artificial (blue) seismograms at each selected station and at each component (Z, R, T). Components that are not used due to noisy or poor recording are left blank.

Table 3.2: The source parameters of 140 earthquakes determined in this study.

| No | Hypocentral Parameters | | | | | | Focal Mechanism Parameters | | | | | | | |
|---|---|---|---|---|---|---|---|---|---|---|---|---|---|---|
| | | | | | | | Nodal Plane 1 | | | Nodal Plane 2 | | | Moment | |
| | Date | Time (GMT) | Lat. (°N) | Lon. (°E) | Depth (km) | Ml | Strike (°) | Dip (°) | Rake (°) | Strike (°) | Dip (°) | Rake (°) | Mw | h (km) |
| 1 | 2006/04/04 | 21:51:52 | 36.9705 | 27.7552 | 17.1 | 3.6 | 58 | 51 | -124 | 285 | 50 | -55 | 3.54 | 12 |
| 2 | 2006/04/17 | 11:53:19 | 36.9848 | 28.2878 | 12.2 | 4.3 | 46 | 58 | -138 | 290 | 55 | -40 | 4.01 | 13 |
| 3 | 2006/04/18 | 01:21:33 | 37.0152 | 28.2658 | 5 | 4 | 48 | 51 | -124 | 275 | 50 | -55 | 3.72 | 11 |
| 4 | 2006/07/31 | 07:35:17 | 36.9538 | 27.8547 | 11 | 3.2 | 66 | 52 | -117 | 285 | 45 | -60 | 3.34 | 13 |
| 5 | 2006/08/09 | 09:18:17 | 37.0487 | 27.9420 | 4 | 3.7 | 105 | 80 | 25 | 10 | 65 | 169 | 3.61 | 16 |
| 6 | 2007/01/31 | 23:13:46 | 36.9847 | 27.7592 | 26 | 3.7 | 244 | 66 | -116 | 115 | 35 | -45 | 3.4 | 13 |
| 7 | 2007/03/06 | 03:34:43 | 37.2195 | 28.4875 | 5 | 4.2 | 275 | 71 | -120 | 155 | 35 | -35 | 3.87 | 13 |
| 8 | 2008/02/01 | 11:59:05 | 36.5455 | 27.2007 | 5 | 4 | 53 | 61 | -99 | 250 | 30 | -75 | 4 | 12 |
| 9 | 2009/01/22 | 09:09:35 | 36.8403 | 27.4768 | 11.6 | 3.4 | 260 | 80 | 60 | 153 | 31 | 161 | 3.55 | 12 |
| 10 | 2009/03/02 | 04:17:58 | 37.1680 | 28.5899 | 7.6 | 3.5 | 315 | 70 | -60 | 76 | 36 | -144 | 3.53 | 11 |
| 11 | 2009/12/30 | 11:00:51 | 36.6400 | 27.9200 | 5.4 | 3.5 | 73 | 76 | -104 | 300 | 20 | -45 | 3.59 | 12 |
| 12 | 2010/06/08 | 19:43:15 | 36.5685 | 27.8965 | 17.3 | 3.4 | 132 | 51 | -98 | 325 | 40 | -80 | 3.3 | 13 |
| 13 | 2010/07/13 | 12:07:51 | 36.9780 | 27.7845 | 14.7 | 3.7 | 55 | 57 | -123 | 285 | 45 | -50 | 3.69 | 10 |
| 14 | 2010/07/15 | 05:35:32 | 36.8280 | 27.3948 | 17.3 | 3.7 | 105 | 70 | -60 | 226 | 36 | -144 | 3.58 | 11 |
| 15 | 2010/07/20 | 21:30:24 | 37.1020 | 27.5883 | 11.4 | 3.7 | 280 | 60 | -70 | 64 | 36 | -121 | 3.77 | 9 |
| 16 | 2010/07/29 | 04:47:41 | 37.1303 | 28.5080 | 5 | 3.7 | 52 | 78 | 112 | 170 | 25 | 30 | 3.76 | 6 |
| 17 | 2010/08/08 | 00:24:11 | 36.6717 | 27.8997 | 8.9 | 4.4 | 59 | 88 | -120 | 325 | 30 | -5 | 4.14 | 15 |
| 18 | 2010/08/08 | 02:12:05 | 36.6717 | 27.8997 | 14.5 | 3.3 | 63 | 77 | -106 | 295 | 20 | -40 | 3.24 | 14 |
| 19 | 2010/09/15 | 04:36:17 | 36.5875 | 27.8958 | 8.9 | 3.9 | 75 | 65 | -90 | 255 | 25 | -90 | 3.91 | 14 |
| 20 | 2011/01/12 | 03:04:03 | 36.8787 | 28.0757 | 9.9 | 3.8 | 65 | 90 | -50 | 155 | 40 | -180 | 3.83 | 12 |
| 21 | 2011/03/15 | 14:50:21 | 37.1780 | 28.3828 | 14.6 | 3.7 | 255 | 80 | 40 | 157 | 51 | 167 | 3.56 | 6 |
| 22 | 2011/04/23 | 03:04:14 | 36.6978 | 28.4397 | 49.2 | 3.9 | 302 | 80 | 165 | 35 | 75 | 10 | 3.55 | 19 |
| 23 | 2011/05/07 | 18:00:49 | 37.0193 | 28.1693 | 6.3 | 4.4 | 60 | 50 | -95 | 248 | 40 | -84 | 3.72 | 3 |
| 24 | 2011/06/15 | 18:23:10 | 36.6065 | 28.8223 | 8.3 | 3.8 | 225 | 50 | 80 | 60 | 41 | 102 | 3.78 | 16 |
| 25 | 2011/06/25 | 07:18:36 | 37.1037 | 27.4295 | 5 | 3.6 | 315 | 70 | -35 | 58 | 57 | -156 | 3.93 | 10 |
| 26 | 2011/10/24 | 10:14:41 | 36.5117 | 28.7085 | 12.7 | 3.9 | 64 | 67 | 153 | 165 | 65 | 25 | 3.88 | 17 |
| 27 | 2012/02/12 | 19:17:32 | 36.8001 | 27.4278 | 11.2 | 4.1 | 110 | 80 | -60 | 217 | 31 | -161 | 3.95 | 11 |
| 28 | 2012/05/08 | 07:31:24 | 37.0601 | 28.5164 | 12.4 | 4.2 | 140 | 65 | 35 | 34 | 59 | 150 | 3.98 | 11 |
| 29 | 2012/05/19 | 12:21:06 | 36.9780 | 27.6207 | 10.8 | 4.4 | 290 | 50 | -70 | 80 | 44 | -112 | 4.16 | 4 |
| 30 | 2012/06/09 | 14:33:14 | 37.0406 | 28.5135 | 12.1 | 4.2 | 86 | 46 | -100 | 280 | 45 | -80 | 3.87 | 3 |
| 31 | 2012/07/18 | 17:46:44 | 37.1611 | 28.3371 | 18.5 | 4.2 | 259 | 60 | -145 | 150 | 60 | -35 | 3.88 | 18 |
| 32 | 2012/10/20 | 01:09:39 | 36.5247 | 28.2904 | 2.7 | 4 | 300 | 55 | 55 | 171 | 48 | 129 | 3.89 | 8 |
| 33 | 2012/11/09 | 04:46:14 | 36.6151 | 27.9547 | 8.1 | 4 | 7 | 75 | 138 | 110 | 50 | 20 | 3.78 | 15 |
| 34 | 2012/11/24 | 21:35:22 | 36.5945 | 27.9312 | 10 | 4 | 205 | 59 | -106 | 55 | 35 | -65 | 3.85 | 12 |
| 35 | 2012/11/24 | 21:04:18 | 36.5520 | 27.9087 | 10.7 | 4.5 | 179 | 86 | -135 | 85 | 45 | -5 | 4.16 | 10 |
| 36 | 2012/11/24 | 21:31:16 | 36.5988 | 27.9098 | 7.5 | 4.3 | 340 | 60 | 125 | 105 | 45 | 45 | 4.15 | 12 |
| 37 | 2012/11/25 | 08:51:46 | 36.6322 | 27.9113 | 6.1 | 4 | 337 | 57 | 130 | 100 | 50 | 45 | 3.94 | 12 |
| 38 | 2012/11/26 | 17:35:42 | 36.6038 | 27.9572 | 11.1 | 4.8 | 204 | 64 | -114 | 70 | 35 | -50 | 4.63 | 12 |
| 39 | 2012/11/26 | 21:20:33 | 36.6383 | 27.9588 | 10.4 | 3.4 | 211 | 76 | -122 | 100 | 35 | -25 | 3.4 | 11 |
| 40 | 2012/11/30 | 02:32:37 | 37.2200 | 28.6237 | 2.1 | 4.2 | 286 | 57 | -103 | 130 | 35 | -70 | 4.1 | 15 |
| 41 | 2012/12/02 | 19:02:57 | 36.6212 | 27.9495 | 5 | 3.9 | 272 | 61 | 132 | 30 | 50 | 40 | 3.85 | 11 |
| 42 | 2013/01/11 | 10:28:23 | 36.5983 | 27.9288 | 5 | 3.8 | 226 | 63 | -127 | 105 | 45 | -40 | 3.69 | 12 |
| 43 | 2013/04/28 | 16:30:53 | 36.9745 | 27.7777 | 7 | 4.2 | 67 | 50 | -113 | 280 | 45 | -65 | 4.11 | 13 |
| 44 | 2013/05/16 | 21:21:19 | 36.9968 | 28.3627 | 4.3 | 4.4 | 305 | 45 | -90 | 125 | 45 | -90 | 4.14 | 3 |
| 45 | 2013/05/16 | 21:26:40 | 37.0017 | 28.3713 | 5 | 4.1 | 305 | 45 | -90 | 125 | 45 | -90 | 3.85 | 3 |
| 46 | 2013/07/17 | 22:00:06 | 37.0558 | 27.9677 | 8.4 | 3.8 | 267 | 62 | -101 | 110 | 30 | -70 | 3.75 | 14 |
| 47 | 2013/07/25 | 23:05:49 | 37.3913 | 26.8655 | 10.7 | 4.2 | 209 | 76 | -164 | 115 | 75 | -15 | 4.1 | 12 |

Table 3.2 cont.: The source parameters of 140 earthquakes determined in this study.

| No | Hypocentral Parameters | | | | | | Focal Mechanism Parameters | | | | | | | |
|---|---|---|---|---|---|---|---|---|---|---|---|---|---|---|
| | | | | | | | Nodal Plane 1 | | | Nodal Plane 2 | | | Moment | |
| | Date | Time (GMT) | Lat. (°N) | Lon. (°E) | Depth (km) | Ml | Strike (°) | Dip (°) | Rake (°) | Strike (°) | Dip (°) | Rake (°) | Mw | h (km) |
| 48 | 2013/10/30 | 03:17:12 | 36.9015 | 27.5683 | 11.2 | 3.9 | 290 | 70 | -40 | 36 | 53 | -155 | 3.81 | 13 |
| 49 | 2014/04/06 | 14:17:15 | 37.0240 | 27.4335 | 6.3 | 3.7 | 57 | 50 | -113 | 270 | 45 | -65 | 3.63 | 8 |
| 50 | 2014/04/10 | 13:24:14 | 37.0277 | 27.4760 | 7.5 | 3.5 | 60 | 80 | -55 | 164 | 36 | -163 | 3.44 | 10 |
| 51 | 2014/04/19 | 23:40:00 | 37.0693 | 28.8837 | 9 | 4 | 315 | 50 | -80 | 120 | 41 | -102 | 4.06 | 14 |
| 52 | 2014/05/01 | 17:33:41 | 37.0317 | 27.4678 | 13.4 | 4.1 | 23 | 58 | -116 | 245 | 40 | -55 | 4.04 | 10 |
| 53 | 2014/05/06 | 09:18:48 | 37.0292 | 27.4733 | 6.8 | 3.7 | 12 | 61 | -118 | 240 | 40 | -50 | 3.67 | 11 |
| 54 | 2014/08/15 | 04:00:17 | 37.0100 | 27.4100 | 8 | 4.1 | 32 | 63 | -121 | 265 | 40 | -45 | 3.93 | 8 |
| 55 | 2014/11/11 | 15:55:19 | 37.1500 | 28.7600 | 9.1 | 3.7 | 315 | 65 | -65 | 87 | 35 | -132 | 3.7 | 10 |
| 56 | 2014/11/11 | 04:46:11 | 37.1258 | 28.7488 | 7 | 3.8 | 310 | 65 | -70 | 89 | 32 | -126 | 3.91 | 10 |
| 57 | 2014/11/24 | 00:25:11 | 37.1353 | 28.4073 | 8.5 | 3.8 | 258 | 57 | -130 | 135 | 50 | -45 | 3.62 | 12 |
| 58 | 2014/12/12 | 05:24:12 | 37.1469 | 28.8152 | 10.4 | 4 | 93 | 45 | -95 | 280 | 45 | -85 | 3.77 | 11 |
| 59 | 2015/03/24 | 22:06:15 | 37.0741 | 28.6353 | 10.9 | 4 | 105 | 55 | -95 | 294 | 35 | -83 | 3.63 | 3 |
| 60 | 2015/06/27 | 05:46:13 | 37.1133 | 28.7683 | 7.4 | 4.2 | 305 | 55 | -80 | 108 | 36 | -104 | 3.65 | 4 |
| 61 | 2015/07/03 | 10:10:27 | 36.9775 | 28.3300 | 6.5 | 4 | 110 | 50 | -70 | 260 | 44 | -112 | 3.89 | 12 |
| 62 | 2015/07/09 | 10:41:36 | 36.8577 | 26.9637 | 7.5 | 4.3 | 15 | 60 | -90 | 195 | 30 | -90 | 4.02 | 12 |
| 63 | 2015/07/19 | 20:22:07 | 37.0338 | 27.4738 | 13.1 | 4.1 | 290 | 65 | -40 | 40 | 54 | -149 | 3.48 | 12 |
| 64 | 2015/07/25 | 18:35:53 | 37.1443 | 28.7117 | 10 | 4 | 340 | 65 | -45 | 93 | 50 | -147 | 3.97 | 8 |
| 65 | 2015/10/20 | 19:00:51 | 36.9269 | 28.0356 | 11.3 | 4 | 226 | 58 | -138 | 110 | 55 | -40 | 3.55 | 12 |
| 66 | 2016/07/19 | 01:55:43 | 37.1385 | 26.9005 | 19.8 | 4 | 110 | 85 | -10 | 201 | 80 | -175 | 3.93 | 13 |
| 67 | 2017/01/25 | 01:19:33 | 36.7400 | 27.6700 | 10.5 | 4.3 | 64 | 64 | -114 | 290 | 35 | -50 | 3.96 | 10 |
| 68 | 2017/03/07 | 04:54:35 | 37.1174 | 28.6184 | 9.8 | 4 | 285 | 65 | 60 | 159 | 38 | 137 | 3.43 | 7 |
| 69 | 2017/05/26 | 16:13:12 | 37.0967 | 28.6496 | 9.5 | 4 | 45 | 70 | -65 | 171 | 32 | -139 | 3.45 | 6 |
| 70 | 2017/07/21 | 00:16:40 | 36.9720 | 27.3210 | 5 | 4.1 | 260 | 65 | -55 | 21 | 42 | -141 | 4.04 | 12 |
| 71 | 2017/07/21 | 00:33:34 | 36.8643 | 27.5957 | 5 | 3.8 | 210 | 90 | -150 | 120 | 60 | 0 | 4 | 11 |
| 72 | 2017/07/21 | 00:57:06 | 36.8597 | 27.6563 | 1 | 4.3 | 270 | 55 | -70 | 58 | 40 | -116 | 4.15 | 9 |
| 73 | 2017/07/21 | 01:17:09 | 36.9390 | 27.5847 | 7.4 | 4 | 85 | 65 | -55 | 206 | 42 | -141 | 3.73 | 11 |
| 74 | 2017/07/21 | 01:25:34 | 36.9722 | 27.4263 | 7.2 | 4 | 255 | 80 | -60 | 2 | 31 | -161 | 3.96 | 14 |
| 75 | 2017/07/21 | 01:50:29 | 36.9870 | 27.3672 | 9.5 | 4.2 | 255 | 80 | -65 | 5 | 27 | -157 | 4.14 | 13 |
| 76 | 2017/07/21 | 03:59:01 | 36.9210 | 27.5783 | 6.7 | 4.4 | 46 | 52 | -117 | 265 | 45 | -60 | 4.21 | 8 |
| 77 | 2017/07/21 | 04:39:23 | 36.9165 | 27.5895 | 2.3 | 3.9 | 65 | 50 | -65 | 209 | 46 | -117 | 3.71 | 8 |
| 78 | 2017/07/21 | 05:13:58 | 36.9120 | 27.6122 | 5 | 4.3 | 93 | 48 | -109 | 300 | 45 | -70 | 4.12 | 8 |
| 79” | 2017/07/21 | 05:52:13 | 36.9823 | 27.3663 | 6.3 | 4.2 | 198 | 69 | -148 | 95 | 60 | -25 | 4.13 | 16 |
| 80 | 2017/07/21 | 09:55:54 | 36.9238 | 27.6480 | 7.1 | 4.1 | 254 | 54 | -110 | 105 | 40 | -65 | 4.18 | 12 |
| 81 | 2017/07/21 | 16:55:24 | 36.9785 | 27.3165 | 9.3 | 3.8 | 250 | 65 | -65 | 22 | 35 | -132 | 3.71 | 15 |
| 82 | 2017/07/22 | 04:53:39 | 36.9502 | 27.5588 | 6.4 | 3.9 | 100 | 60 | -60 | 231 | 41 | -131 | 3.65 | 8 |
| 83 | 2017/07/22 | 00:34:12 | 36.9467 | 27.5355 | 6.4 | 4.1 | 275 | 50 | -65 | 59 | 46 | -117 | 3.8 | 4 |
| 84 | 2017/07/22 | 17:09:20 | 36.9608 | 27.2730 | 5.7 | 4.5 | 285 | 55 | -65 | 66 | 42 | -121 | 4.49 | 13 |
| 85 | 2017/07/23 | 23:18:29 | 36.9497 | 27.5868 | 5 | 3.8 | 217 | 85 | -155 | 125 | 65 | -5 | 3.59 | 10 |
| 86 | 2017/07/24 | 21:48:47 | 36.9730 | 27.4732 | 5 | 4 | 80 | 70 | -92 | 265 | 20 | -85 | 3.94 | 10 |
| 87 | 2017/07/29 | 23:08:43 | 36.9135 | 27.3805 | 5 | 3.4 | 55 | 60 | -125 | 290 | 45 | -45 | 3.4 | 8 |
| 88 | 2017/07/30 | 10:56:32 | 36.9902 | 27.5850 | 5 | 4.1 | 260 | 55 | -60 | 35 | 45 | -126 | 3.83 | 8 |
| 89 | 2017/07/30 | 07:02:12 | 36.9897 | 27.5872 | 5 | 4.4 | 285 | 65 | -50 | 42 | 46 | -144 | 4.2 | 8 |
| 90 | 2017/07/31 | 16:25:36 | 36.9815 | 27.6020 | 4.3 | 4.1 | 270 | 50 | -70 | 60 | 44 | -112 | 3.83 | 9 |
| 91 | 2017/08/07 | 05:44:25 | 36.9750 | 27.5985 | 5 | 4.2 | 290 | 55 | -45 | 50 | 55 | -135 | 4.02 | 9 |
| 92 | 2017/08/07 | 18:25:57 | 36.9893 | 27.6432 | 5.9 | 4 | 247 | 50 | -113 | 100 | 45 | -65 | 4.17 | 9 |
| 93 | 2017/08/08 | 01:46:19 | 37.0088 | 27.6247 | 5 | 4.5 | 285 | 60 | -80 | 86 | 31 | -107 | 4.34 | 8 |
| 94 | 2017/08/09 | 22:56:18 | 36.9843 | 27.6537 | 6.6 | 4.2 | 265 | 60 | -80 | 66 | 31 | -107 | 3.88 | 8 |

Table 3.2 cont.: The source parameters of 140 earthquakes determined in this study.

| No | Hypocentral Parameters | | | | | | Focal Mechanism Parameters | | | | | | | |
|---|---|---|---|---|---|---|---|---|---|---|---|---|---|---|
| | | | | | | | Nodal Plane 1 | | | Nodal Plane 2 | | | Moment | |
| | Date | Time (GMT) | Lat. (°N) | Lon. (°E) | Depth (km) | Ml | Strike (°) | Dip (°) | Rake (°) | Strike (°) | Dip (°) | Rake (°) | Mw | h (km) |
| 95 | 2017/08/13 | 13:37:43 | 37.1240 | 27.6895 | 7.1 | 3.7 | 120 | 60 | -60 | 251 | 41 | -131 | 3.66 | 11 |
| 96 | 2017/08/13 | 14:24:32 | 37.1108 | 27.7005 | 5 | 3.8 | 236 | 66 | -129 | 120 | 45 | -35 | 3.57 | 11 |
| 97 | 2017/08/13 | 17:09:06 | 37.1193 | 27.7060 | 6.4 | 4 | 110 | 70 | -75 | 252 | 25 | -125 | 3.79 | 8 |
| 98 | 2017/08/14 | 11:25:23 | 37.1220 | 27.7333 | 2.8 | 3.6 | 239 | 64 | -134 | 125 | 50 | -35 | 3.73 | 11 |
| 99 | 2017/08/18 | 12:47:32 | 36.9400 | 27.5800 | 5 | 4.1 | 285 | 50 | -90 | 105 | 40 | -90 | 4.24 | 8 |
| 100 | 2017/09/08 | 23:23:32 | 37.1650 | 27.7228 | 8 | 4 | 100 | 85 | -25 | 192 | 65 | -174 | 3.91 | 12 |
| 101 | 2017/10/05 | 20:41:25 | 37.2397 | 28.0560 | 5.7 | 3.6 | 145 | 65 | -45 | 258 | 50 | -147 | 3.51 | 10 |
| 102 | 2017/10/09 | 00:56:40 | 36.9475 | 27.6788 | 1.9 | 3.4 | 275 | 50 | -65 | 59 | 46 | -117 | 3.49 | 9 |
| 103 | 2017/10/14 | 14:02:32 | 36.9380 | 27.6793 | 5.5 | 3.7 | 270 | 50 | -70 | 60 | 44 | -112 | 3.72 | 9 |
| 104 | 2017/10/22 | 05:36:03 | 37.0085 | 27.6612 | 5.5 | 3.6 | 130 | 70 | 80 | 337 | 22 | 116 | 3.52 | 9 |
| 105 | 2017/12/30 | 19:12:49 | 37.1127 | 28.6485 | 5 | 3.9 | 46 | 60 | 145 | 155 | 60 | 35 | 3.84 | 17 |
| 106 | 2018/01/05 | 04:33:17 | 37.1145 | 28.6365 | 8.5 | 4.2 | 295 | 50 | -90 | 115 | 40 | -90 | 3.97 | 2 |
| 107 | 2018/01/13 | 21:31:14 | 37.0003 | 27.6250 | 5.8 | 3.6 | 71 | 67 | -153 | 330 | 65 | -25 | 3.62 | 22 |
| 108 | 2018/01/17 | 22:06:38 | 37.0870 | 28.5933 | 5 | 3.6 | 335 | 65 | -40 | 85 | 54 | -149 | 3.48 | 7 |
| 109 | 2018/04/20 | 12:20:09 | 36.9370 | 27.3095 | 11.8 | 3.9 | 63 | 56 | -113 | 280 | 40 | -60 | 3.74 | 8 |
| 110 | 2018/05/01 | 04:03:48 | 36.9063 | 27.5685 | 3.5 | 4.2 | 269 | 65 | -95 | 100 | 25 | -80 | 4.05 | 8 |
| 111 | 2018/06/09 | 22:24:52 | 36.9065 | 27.5923 | 13.3 | 4 | 255 | 55 | -120 | 120 | 45 | -55 | 3.97 | 14 |
| 112 | 2018/07/02 | 23:25:26 | 37.2138 | 28.2968 | 5 | 3.4 | 55 | 73 | 148 | 155 | 60 | 20 | 3.41 | 13 |
| 113 | 2018/10/15 | 14:21:23 | 36.8792 | 27.5695 | 7.2 | 4 | 75 | 88 | -115 | 340 | 25 | -5 | 4.1 | 14 |
| 114 | 2018/11/05 | 18:07:57 | 37.1702 | 28.7945 | 7.5 | 3.7 | 274 | 54 | -110 | 125 | 40 | -65 | 3.67 | 16 |
| 115 | 2019/02/11 | 16:38:03 | 36.5225 | 28.8355 | 10.7 | 4 | 125 | 70 | -50 | 237 | 44 | -150 | 3.97 | 17 |
| 116 | 2019/03/16 | 13:50:12 | 37.1595 | 28.6928 | 5 | 3.7 | 72 | 45 | -85 | 245 | 45 | -95 | 3.51 | 2 |
| 117 | 2019/05/19 | 14:47:13 | 36.8607 | 26.7655 | 20.9 | 3.8 | 305 | 90 | 40 | 215 | 50 | 180 | 3.86 | 16 |
| 118 | 2019/05/26 | 12:07:10 | 37.2740 | 28.0373 | 15.1 | 4.2 | 298 | 62 | -79 | 95 | 30 | -110 | 4.19 | 17 |
| 119 | 2019/10/22 | 12:23:05 | 36.7413 | 27.1875 | 9.9 | 3.8 | 247 | 51 | -98 | 80 | 40 | -80 | 3.73 | 9 |
| 120 | 2020/03/13 | 21:57:52 | 36.9832 | 27.3657 | 11.4 | 3.8 | 244 | 68 | -118 | 120 | 35 | -40 | 3.93 | 13 |
| 121 | 2020/03/17 | 18:14:31 | 36.9605 | 27.3438 | 15.8 | 4.3 | 260 | 65 | -45 | 13 | 50 | -147 | 4.16 | 16 |
| 122 | 2021/03/15 | 01:55:48 | 37.1548 | 28.7873 | 6.4 | 4.3 | 130 | 75 | -45 | 235 | 47 | -159 | 4.1 | 12 |
| 123 | 2021/10/11 | 20:36:27 | 36.5153 | 27.0707 | 7.4 | 3.5 | 359 | 76 | 154 | 95 | 65 | 15 | 3.7 | 11 |
| 124 | 2021/11/15 | 21:34:57 | 36.9460 | 27.6922 | 6.4 | 3.4 | 345 | 65 | 40 | 235 | 54 | 149 | 3.44 | 8 |
| 125 | 2021/12/09 | 15:06:44 | 36.5238 | 28.7797 | 19.5 | 3.5 | 232 | 85 | -160 | 140 | 70 | -5 | 3.47 | 21 |
| 126 | 2022/02/11 | 16:18:07 | 36.9642 | 27.6658 | 7.7 | 4.2 | 47 | 77 | 149 | 145 | 60 | 15 | 3.89 | 9 |
| 127 | 2022/02/24 | 14:50:34 | 37.0675 | 28.3710 | 3.2 | 3.9 | 28 | 62 | 139 | 140 | 55 | 35 | 3.92 | 13 |
| 128 | 2022/02/25 | 01:03:59 | 37.0690 | 28.5628 | 6.7 | 3.5 | 140 | 60 | -50 | 261 | 48 | -138 | 3.6 | 15 |
| 129 | 2022/03/09 | 07:05:11 | 36.9147 | 27.9647 | 7.3 | 3.6 | 81 | 71 | -83 | 240 | 20 | -110 | 3.35 | 14 |
| 130 | 2022/03/13 | 18:41:54 | 37.0175 | 28.3885 | 8 | 3.6 | 63 | 68 | -125 | 305 | 40 | -35 | 3.56 | 11 |
| 131 | 2022/04/29 | 17:35:33 | 37.0533 | 28.2308 | 11.5 | 3.8 | 140 | 60 | -40 | 253 | 56 | -143 | 3.79 | 14 |
| 132 | 2022/06/14 | 00:13:04 | 36.7800 | 28.0600 | 6.1 | 3.6 | 75 | 75 | -70 | 200 | 25 | -142 | 3.47 | 17 |
| 133 | 2022/06/14 | 00:07:38 | 36.7498 | 28.0660 | 7.3 | 3.6 | 65 | 75 | -75 | 199 | 21 | -134 | 3.48 | 17 |
| 134 | 2022/06/14 | 00:41:52 | 36.7770 | 28.0617 | 5.7 | 3.5 | 70 | 70 | -85 | 236 | 21 | -103 | 3.39 | 17 |
| 135 | 2022/09/04 | 17:00:18 | 37.1168 | 28.5158 | 4 | 3.1 | 258 | 57 | -130 | 135 | 50 | -45 | 3.07 | 8 |
| 136 | 2022/09/04 | 17:47:51 | 37.1085 | 28.5402 | 3.4 | 3.9 | 49 | 67 | 153 | 150 | 65 | 25 | 3.85 | 10 |
| 137 | 2022/09/05 | 10:54:43 | 37.1332 | 28.5120 | 5 | 3.2 | 155 | 65 | -30 | 259 | 63 | -152 | 3.29 | 12 |
| 138 | 2022/09/05 | 13:45:54 | 37.1075 | 28.5117 | 2.8 | 3.7 | 247 | 62 | -139 | 135 | 55 | -35 | 3.55 | 9 |
| 139 | 2022/09/27 | 17:06:41 | 36.9415 | 27.8317 | 7 | 3.9 | 250 | 55 | -120 | 115 | 45 | -55 | 3.64 | 16 |
| 140 | 2022/10/02 | 10:58:01 | 37.0373 | 28.8992 | 5 | 4.6 | 95 | 60 | -40 | 208 | 56 | -143 | 4.59 | 12 |

# 4. STRESS TENSOR ANALYSIS

## 4.1. Stress Tensor Inversion

The stress tensor inversion method is used to identify the direction of the best fitting stress tensor for a given region based on the FMS of the fault plane. There are various stress tensor inversion methods found from the focal mechanism solutions [81]-[90]. These methods often assume that (1) tectonic stress in the region is uniform (homogeneous), (2) earthquakes occur on pre-existing faults of varied orientations, and (3) the slip vector is oriented in the shear stress direction. If these assumptions are met, the stress inversion methods are able to determine four parameters of the stress tensor: three angles indicating the principal stresses ($\sigma_1, \sigma_2, \sigma_3$) and shape ratio (R). The stress tensor is expressed by the three main stress axes. $\sigma_1$ is the maximum, $\sigma_2$ is the intermediate and $\sigma_3$ is the minimum compressive stress axis. When $\sigma_1$ is the vertical axis, extension type; $\sigma_2$ is the vertical axis, strike-slip type; $\sigma_3$ is the vertical axis, compression type regime is seen. The stress ratio according to the positioning of these three axes (R),

$$R = (\sigma_1 - \sigma_2) / (\sigma_1 - \sigma_3) \tag{4.1}$$

In this study, Michael's method is used (Michael, 1984;1987) [86], [85]. Michael's Method is a linear inversion method that does not require a fault plane to be defined. It uses the bootstrap resampling method to select the fault plane from the nodal planes. The STRESSINVERSE program based on a modified version of Michael's Method developed by Vavrycuk [2014] is used for stress inversion in this study. The principal stress axes and the regional stress ratio (R) are determined iteratively in order to define an accurate stress field.

## 4.2. Determination of the Tectonic Domain

In order to analyze the stress field orientation at the GofG, 140 fault plane solutions have been used and the stress axes orientation are determined by using STRESSINVERSE program.

The orientations of the P- and T-axes are categorized according to Zoback [1992] tectonic regime assignment (Table 4.1).

Table 4.1: Tectonic regime assignment [91].The regime types can explain as NF = normal faulting, NS = predominantly normal faulting with strike–slip component, SS = strike-slip faulting, TS = predominantly thrust faulting with strike–slip component, TF = thrust faulting.

| P/S1-axis | B/S2-axis | T/S3-axis | Regime | SH-azimuth |
|---|---|---|---|---|
| pl > 52 | | pl < 35 | NF | azim. of B-axis |
| 40 < pl < 52 | | pl < 20 | NS | azim. of T-axis + 90° |
| pl < 40 | pl > 45 | pl < 20 | SS | azim. of T-axis + 90° |
| pl < 20 | pl > 45 | pl < 40 | SS | azim. of P-axis |
| pl < 20 | | 40 < pl < 52 | TS | azim. of P-axis |
| pl < 35 | | pl > 52 | TF | azim. of P-axis |

The principal stress (PS) directions of the whole area are found in azimuth/plunge which are $\sigma_1$ = 76°/77°, $\sigma_2$ = 261°/13°, $\sigma_3$ =171°/1°, respectively (Figure 4.1). The shape ratio (stress magnitude ratio) (R) of the area is found 0.24 which gives information about the relative stress magnitude of the principal stresses. The principal stress $\sigma_1$ is positioned in vertical which represents the normal faulting regime. The confidence angle of the PS axes and a ternary diagram are also shown. In the ternary diagram, each vertex of the triangle represents pure strike-slip, normal and thrust faulting.

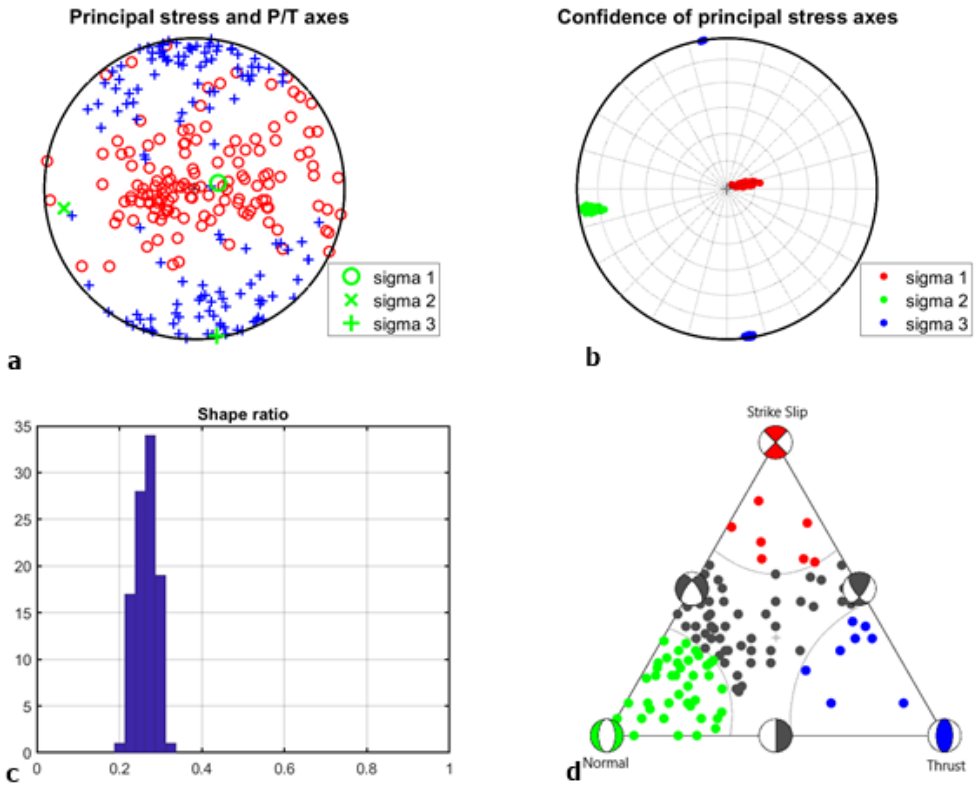


Figure 4.1: The stress inversion results of entire area a) Distribution of P (red circles) and T (blue pluses) axes orientation b) stress axes c) shape ratio d) focal mechanisms on a ternary diagram.

The distribution of FMS and the complex tectonic features of the region suggest that examining the region as a whole leads to oversimplified conclusions. Consequently, the study area was divided into sub-regions according to the differences in FMSs, fault types, tectonic settings, locations, and seismic depths. The first three regions include subregions 1, 2 and 3 and the most dominant feature emphasized in these regions is geographic proximity. The last three regions include sub-regions 4,5 and 6 presents variation of the results with respect to depth. Thus, we are able to investigate the stress parameters and discover local changes in these parameters. As illustrated in Figure 4.2, the the region is divided into three sub-regions due to location. The other three sub-groups are divided into 0-8 km, 8-19 km and 19-40 km ranges according to the depth of seismicity.

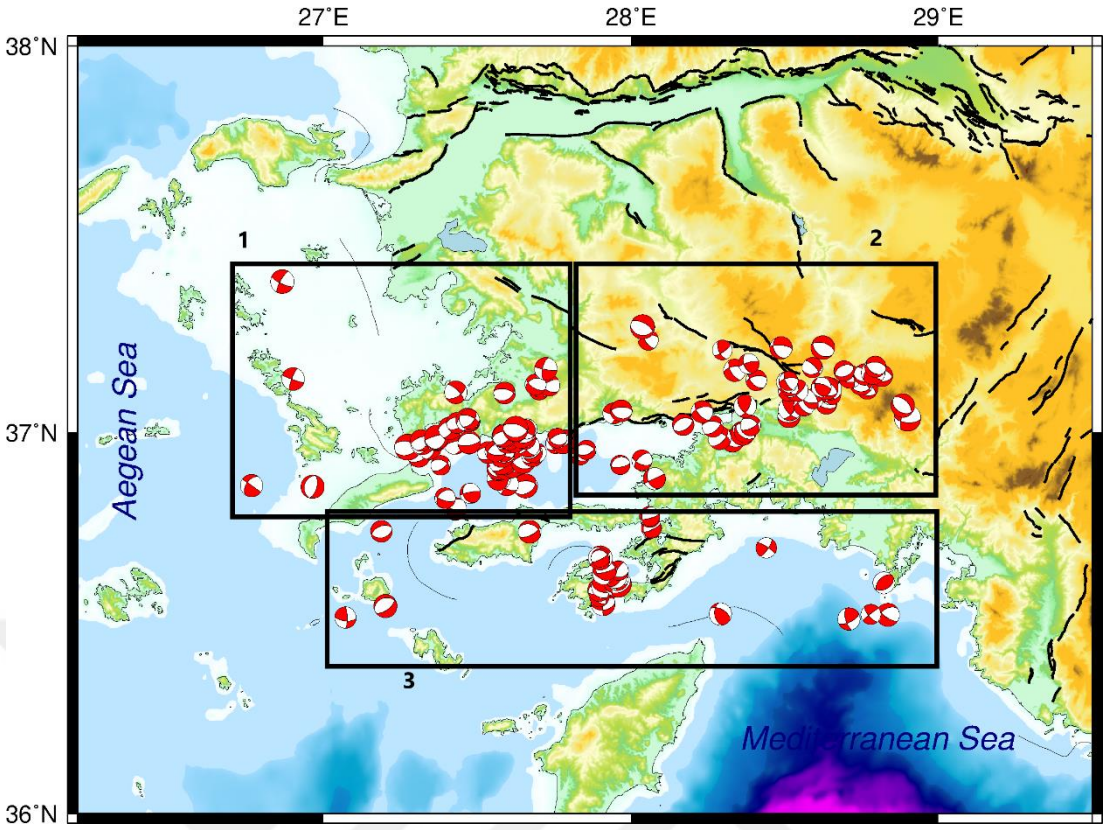


Figure 4.2: The map demonstrates the sub-regions of the Gulf of Gökova

Sub-region 1 covers the western part of the Gulf of Gökova, including Bodrum. Although concentrated around Bodrum and Çökertme, the region includes focal mechanism of 64 earthquakes. The PS directions of the sub-region 1 are found in azimuth/plunge which are $\sigma_1$ = 260°/79°, $\sigma_2$ = 76°/10°, $\sigma_3$ =166°/0° azimuth/plunge respectively. The shape ratio (stress magnitude ratio) (R) of the area is found 0.24 which gives information about the relative stress magnitude of the principal stresses. Figure 4.3 depicts the distribution of focal mechanisms. The region is characterized by normal faulting ENE-WSW oriented compression and NNW-SSE directed extension as a result of stress tensor solutions (Figure 4.4a). The maximum PS $\sigma_1$ is vertical by trending in ENE-WSW and $\sigma_3$ is sub-horizontal with NNW-SSE trend. The ternary diagram in Figure 4.4d confirms that the majority of the earthquakes that occurred in the sub-region are in normal faulting regime.

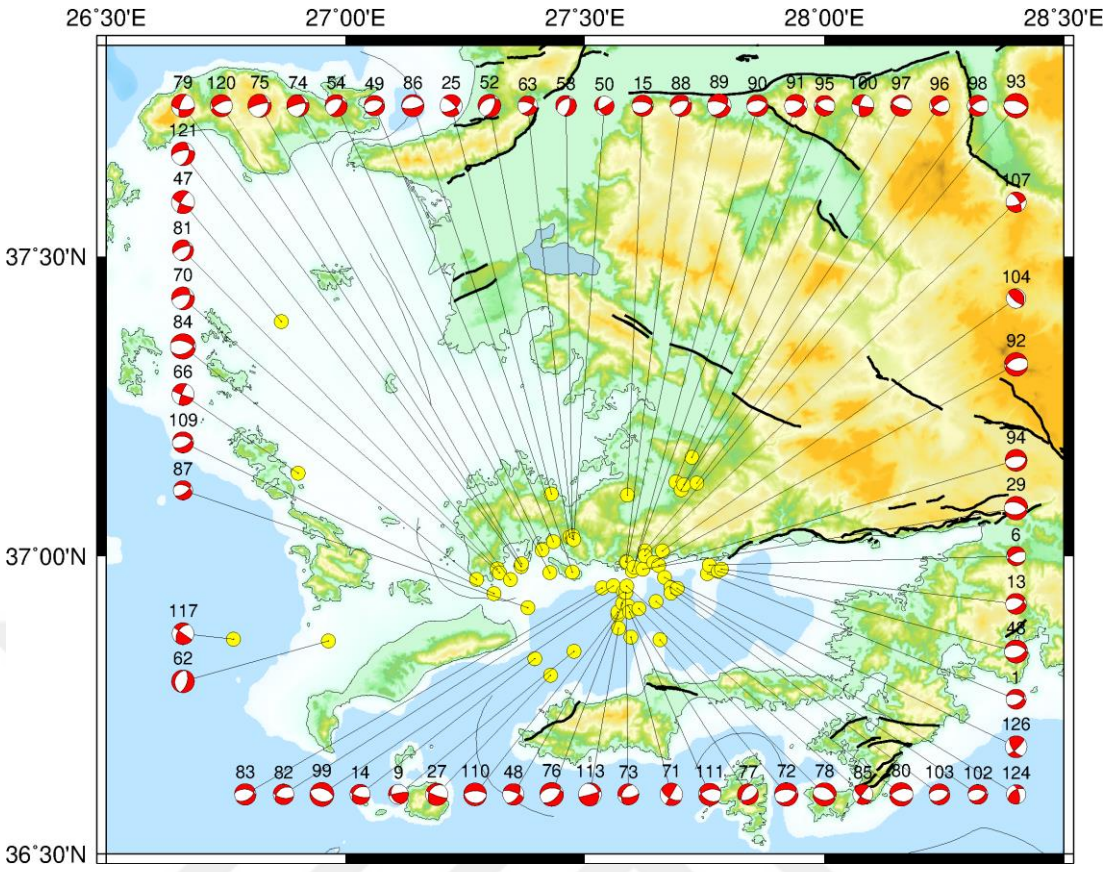


Figure 4.3: The map demonstrates the sub-region1 of the Gulf of Gökova

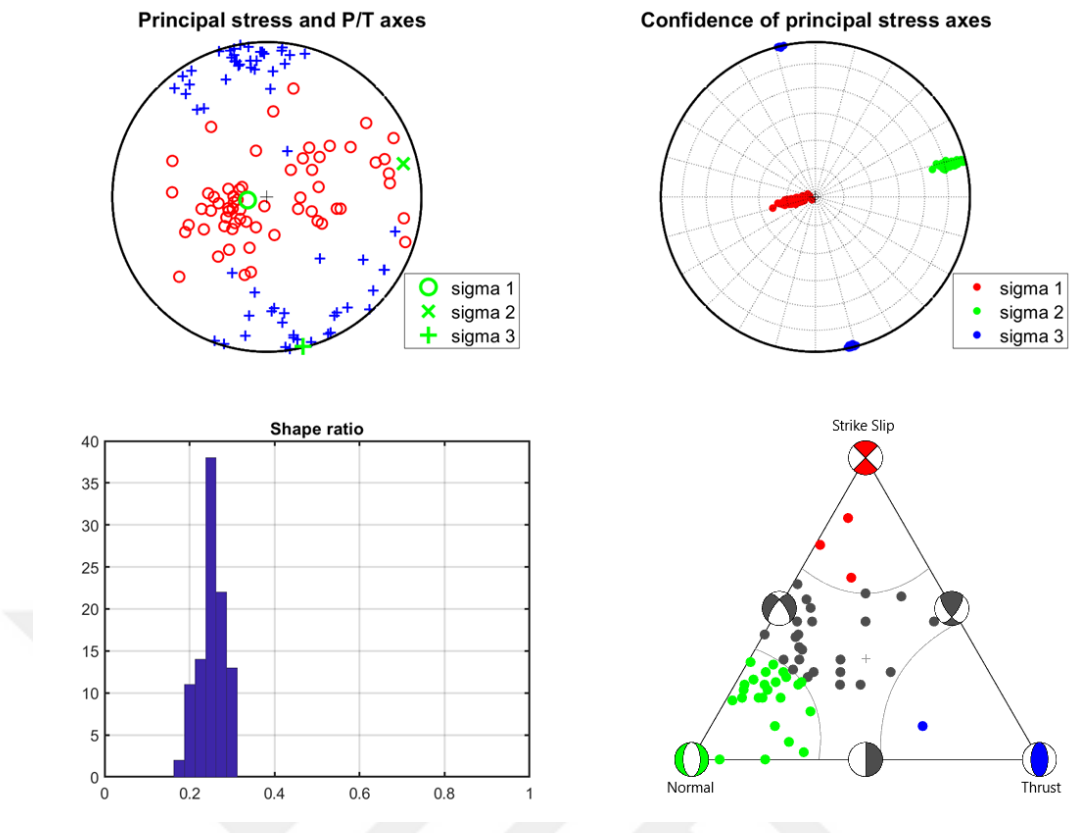


Figure 4.4: The stress inversion results of sub-region1 a) Distribution of P (red circles) and T (blue pluses) axes orientation b) stress axes c) shape ratio d) ternary diagram

The sub-region 2, which includes the earthquakes around mainly Ören, Ula and Muğla, forms the eastern part of the Gulf of Gökova. Total number of 49 earthquakes are interpreted for this subregion. The PS directions of the sub-region2 are found in azimuth/plunge which are $\sigma_1$ = 109°/80°, $\sigma_2$ = 278°/9°, $\sigma_3$ =8°/1° respectively. The shape ratio (R) of the area is found 0.25. Figure 4.5 demonstrates the distribution of focal mechanisms. The region is characterized by normal faulting WNW-ESE oriented compression and NNE-SSW directed extension due to stress tensor solutions (Figure 4.6a). $\sigma_1$ principal stress is vertical by trending in ESE-WNW and $\sigma_3$ is sub-horizontal by trending in NNE-SSW. The ternary diagram in Figure 4.6d confirms that the majority of the earthquakes that occurred in the sub-region are in normal faulting regime.

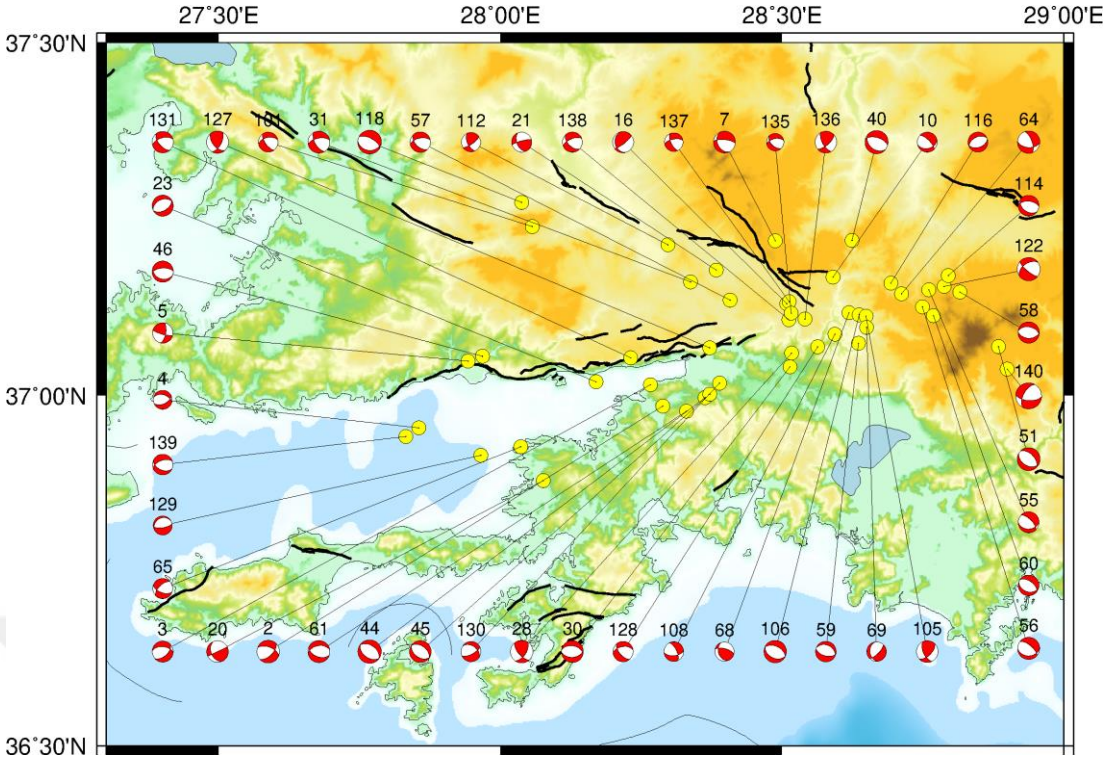


Figure 4.5: The map demonstrates the sub-region2 of the Gulf of Gökova

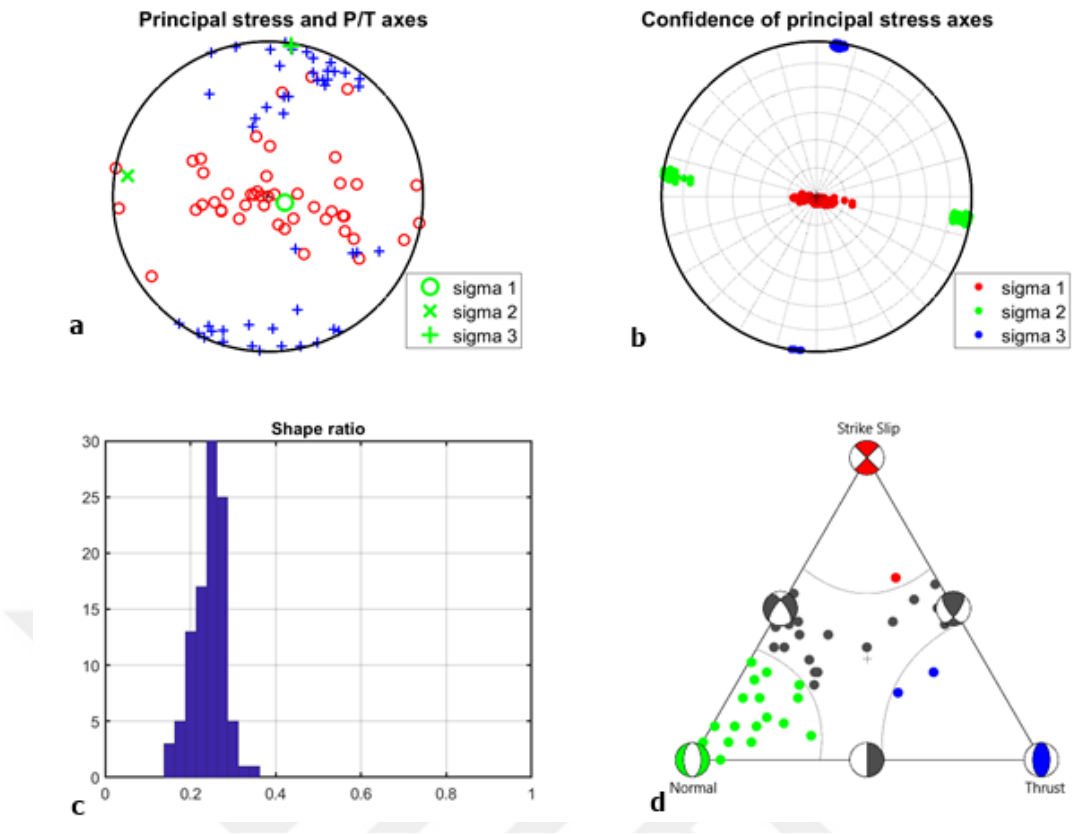


Figure 4.6: The stress inversion results of sub-region2 a) Distribution of P (red circles) and T (blue pluses) axes orientation b) stress axes c) shape ratio d) ternary diagram

In the sub-region 3, which includes the southern part of the GofG, clustered earthquake activity around Bozburun is noticeable. The region covers Datça, Marmaris and Köyceğiz. A total of 27 earthquakes are interpreted in this area, which is the area with the least seismic activity according to locations in each sub-region. The PS directions of the sub-region3 are found in azimuth/plunge which are $\sigma_1$ = 56°/47, $\sigma_2$ = 272°/36°, $\sigma_3$ =167°/18° respectively. The shape ratio (R) of the area is found 0.73. The regime is mainly normal faulting with strike slip component according to Zoback [1992] tectonic regime assignment criteria. Figure 4.7 demonstrates the distribution of focal mechanisms. The region is characterized by NE oriented compression and NNW-SSE directed extension due to stress tensor solutions (Figure 4.8a). The PS $\sigma_1$ is sub-horizontal by trending in NE and $\sigma_3$ is sub-horizontal by trending in NNW-SSE. The ternary diagram in Figure 4.8d confirms that the sub-region is under the control of complex tectonic regime.

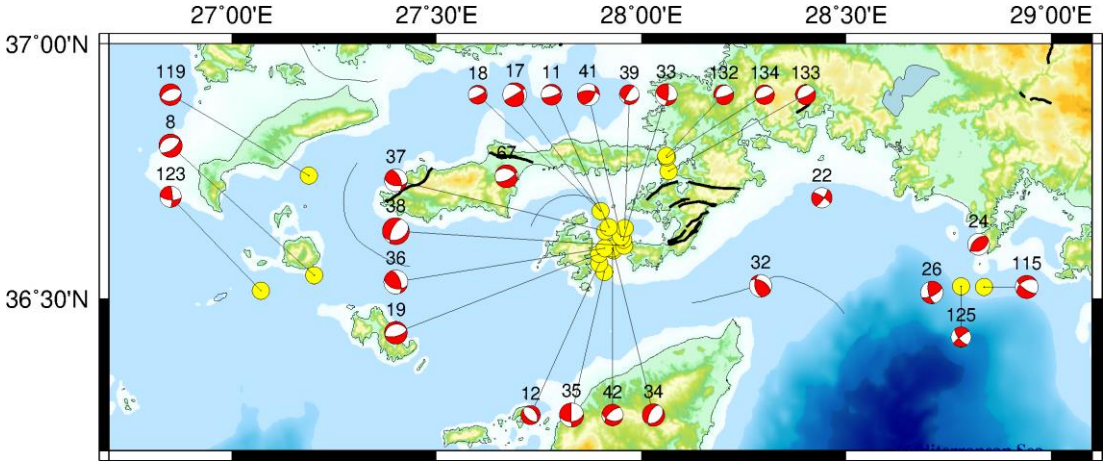


Figure 4.7: The map demonstrates the sub-region3 of the Gulf of Gökova

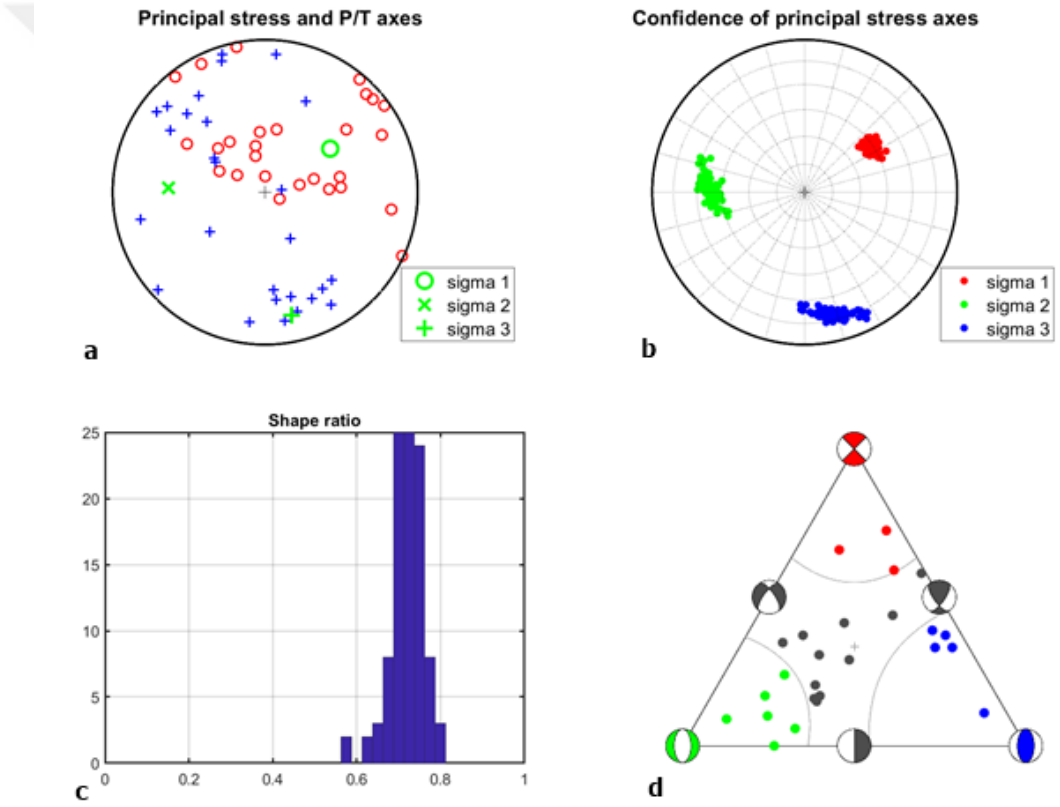


Figure 4.8: The stress inversion results of sub-region3 a) Distribution of P (red circles) and T (blue pluses) axes orientation b) stress axes c) shape ratio d) ternary diagram

The sub-region 4, which includes the earthquakes at a depth of 0-8 km of the the Gulf of Gökova, clustered earthquake activity around Çökertme towards the direction of Datça is noticeable. In terms of seismic activity, other remarkable parts

can be shown as Ula-Muğla and around Bodrum. A total of 84 earthquakes are interpreted in this area. The distribution of focal mechanisms is shown in Figure 4.9. The PS directions of the sub-region4 are found in azimuth/plunge which are σ1 = 88°/72, σ2 = 260°/17°, σ3 =351°/2° respectively. The shape ratio (stress magnitude ratio) (R) of the area is found 0.16. The region is characterized by normal faulting with E-W oriented compression and NNW-SSE directed extension due to stress tensor solutions (Figure 4.10a). The PS σ1 is vertical by trending in E-W and σ3 is sub-horizontal by trending in NNW-SSE. The ternary diagram in Figure 4.10d also indicates that the majority of the earthquakes that occurred in the sub-region are in normal faulting regime.

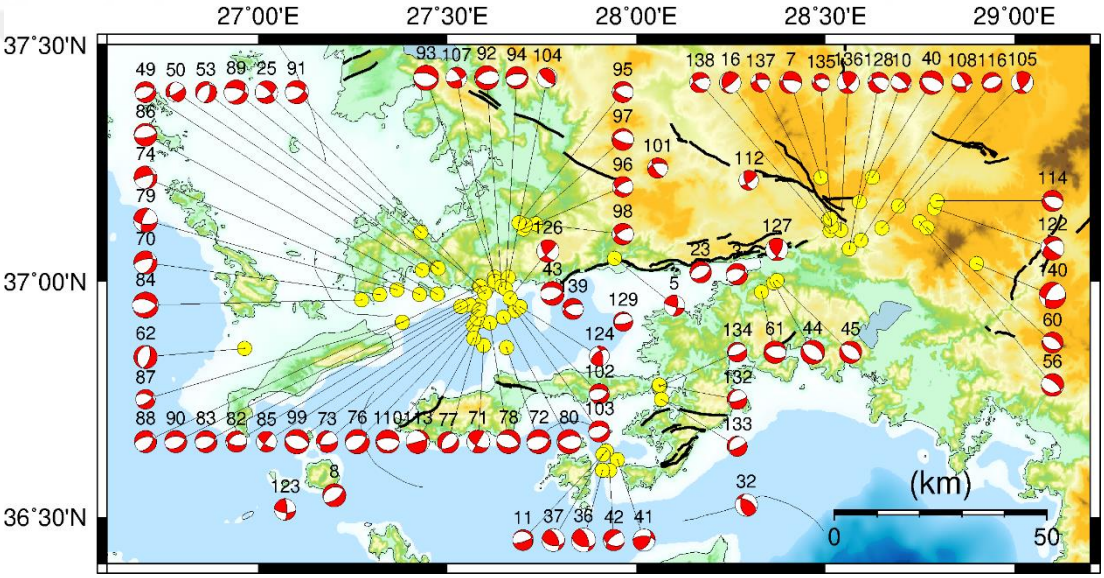


Figure 4.9: The map demonstrates the sub-regions4 (0-8 km) of the Gulf of Gökova

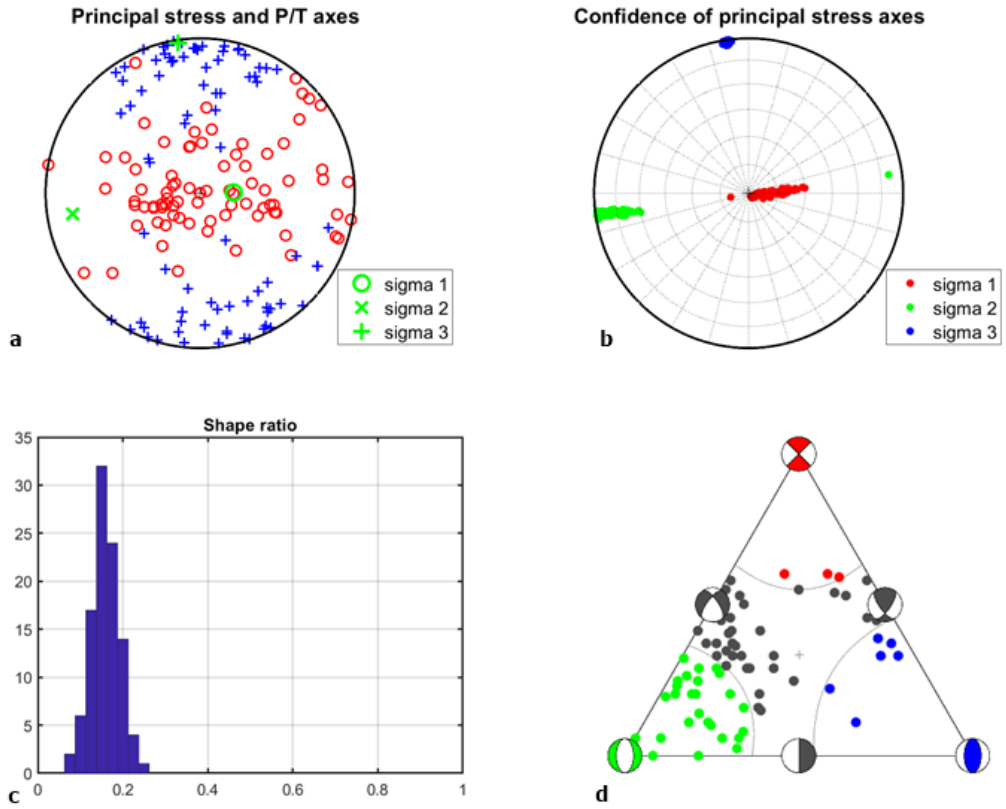


Figure 4.10: The stress inversion results of sub-region4 a) Distribution of P (red circles) and T (blue pluses) axes orientation b) stress axes c) shape ratio d) ternary diagram

In the sub-region 5, which includes the earthquakes at a depth of 8-19 km, the seismic activity is clustered around Bodrum, Bozburun and Ula-Muğla. A total number of 54 earthquakes are interpreted in this area. Figure 4.11 demonstrates the distribution of focal mechanisms. The PS directions of the sub-region5 are found in azimuth/plunge which are σ1 = 348°/84, σ2 = 258°/0°, σ3 =168°/5° respectively. The shape ratio (R) of the area is found 0.16. The region is characterized by normal faulting with E-W oriented compression and NNW-SSE directed extension due to stress tensor solutions (Figure 4.12a). The PS σ1 is vertical by trending in E-W and σ3 is sub-horizontal by trending in NNW-SSE. The ternary diagram in Figure 4.12d confirms that the majority of the earthquakes that occurred in the sub-region are in normal faulting regime.

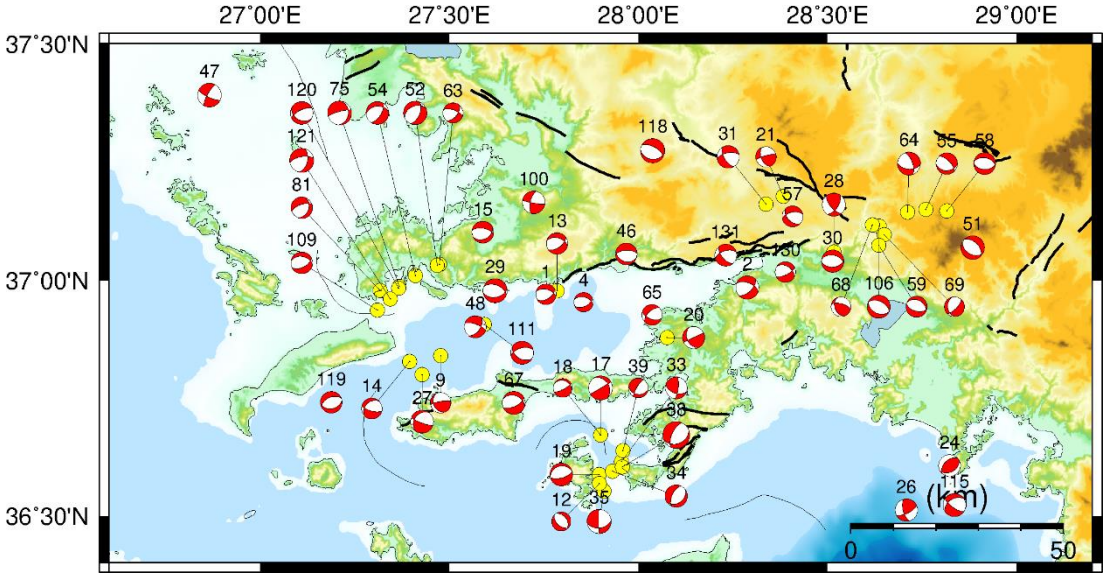


Figure 4.11: The map demonstrates the sub-regions5 (8-19 km) of the Gulf of Gökova

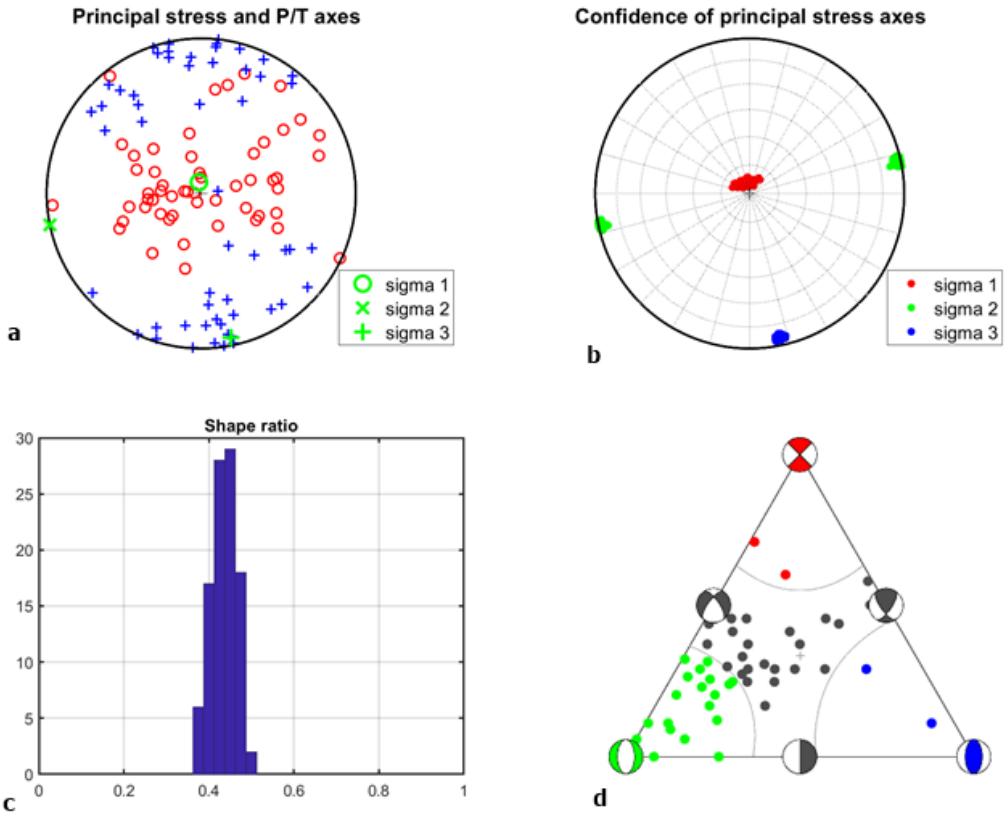


Figure 4.12: The stress inversion results of sub-region5 a) Distribution of P (red circles) and T (blue pluses) axes orientation b) stress axes c) shape ratio d) ternary diagram

In the sub-region 6 covers the earthquakes at a depth of 19 and below of the GofG. Here, the earthquakes are more scattered and few in number and all of are located offshore. A total of 5 earthquakes are shown in Figure 4.13. However, the number of earthquakes is not sufficient enough for inversion process. Figure 4.14 shows the distribution of the earthquake-types in this sub-region. It can be determined that the strike-slip type is the majority.

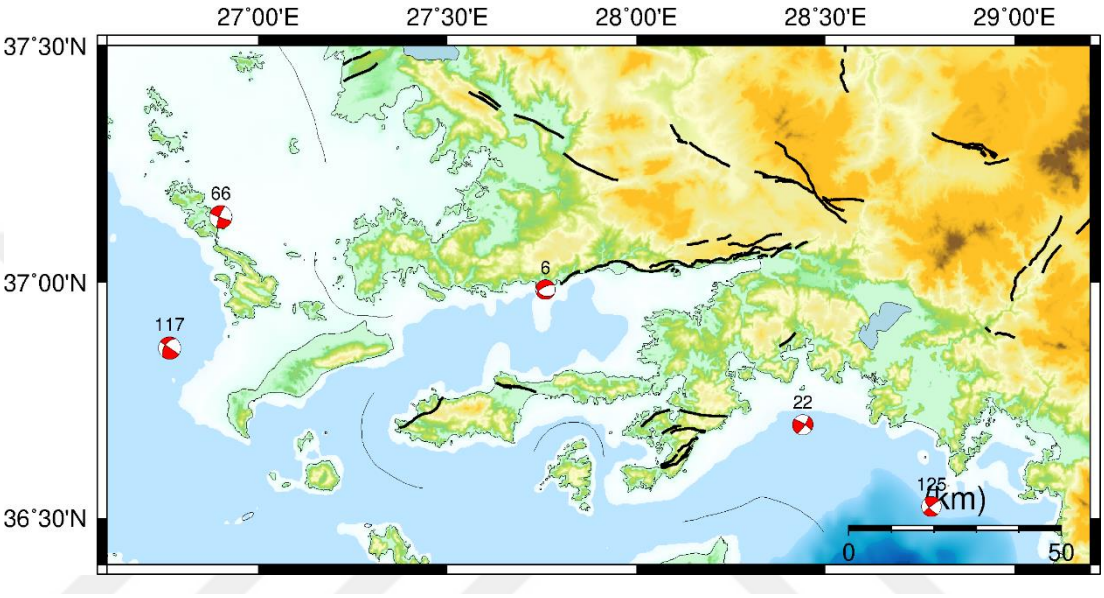


Figure 4.13: The map demonstrates the sub-region6 (19 and below km) of the Gulf of Gökova

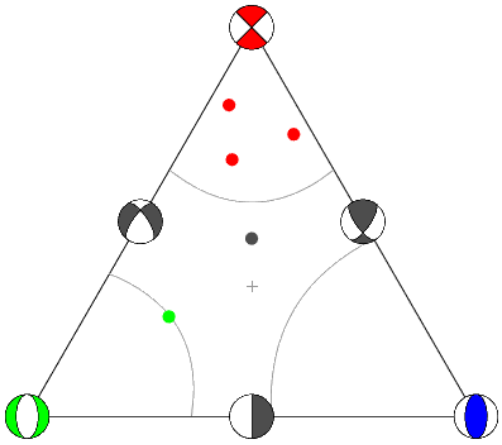

Figure 4.14: Ternary diagram of the earthquakes with depth of 19 km and below.

# 5. DISCUSSION AND CONCLUSION

In this study, a total number of 140 M ≥ 3.0 earthquakes that occured between the years 2006 and 2022, in the Gulf of Gökova and its surroundings were analyzed using the moment tensor [Herrmann, 2013] and stress tensor inversion [Vavryčuk, 2014] methods.

The results show that the normal faulting mechanism is prominent in the region, while the reverse faulting mechanism is rare. The observed P- and T-axis orientations indicate that the region is compressed in the E-W direction and extended in the NNW-SSE direction. This is consistent with the tectonic regime of W Anatolia.

Due to the dense assemblage of focal mechanism solutions, fault types, tectonic settings, locations, and seismic depths, the study area was divided into sub-regions for simplicity. By using STRESSINVERSE program, each region (except for the last sub-region) is examined to determine its stress patterns. In sub-region1, $\sigma_1$ principal stress is vertical with ENE-WSW trend and $\sigma_3$ is sub-horizontal with NNW-SSE trend, indicating normal faulting. In sub-region2, the principal stress $\sigma_1$ is vertical by trending in ESE-WNW and $\sigma_3$ is sub-horizontal in trending in NNE-SSW, indicating normal faulting. Sub-region3 is identified with a more complex regime than other subregions. In this sub-region $\sigma_1$ principal stress is sub-horizontal with a trend in NE and $\sigma_3$ is sub-horizontal with a trend in NNW-SSE, which indicates normal faulting with strike-slip components. In sub-region4, the principal stress $\sigma_1$ is vertical trending in ENE-WSW and $\sigma_3$ is sub-horizontal trending in NNW-SSE, indicates normal faulting. In sub-region5 $\sigma_1$ principal stress is vertical trending in ENE-WSW and $\sigma_3$ is sub-horizontal trending in NNW-SSE, indicating normal faulting.

Considering the distribution of the analyzed earthquakes in terms of source parameters, 79% are results of normal faults or oblique faults with a high normal component ratio,12 % by strike-slip faults or oblique faults with a high strike-slip component ratio and 9% by reverse faults or oblique faults with a high reverse component ratio. In addition, the focal mechanisms obtained by moment tensor inversion of these earthquakes are consistent with the tectonic structures in the regions.

Figure 5.1 shows the tectonic stress field of the region as presented in World Stress Map (WSM) data, which is based on the web-based source application CASMO [92]. According to WSM the Gulf of Gökova and its surroundings are under the control of counterclockwise normal faulting, which is consistent with the result of this study.

Considering the distribution of the analyzed earthquakes in terms of source parameters, 79% are caused by normal faults or oblique faults with a high normal component ratio,12 % by strike-slip faults or oblique faults with a high strike-slip component ratio and 9% by reverse faults or oblique faults with a high reverse component ratio. In addition, the focal mechanisms obtained by moment tensor inversion of these earthquakes are consistent with the tectonic structures in the regions where they occur.

Figure 5.1 shows the results of the stress field with the tectonic stress field, regime types are shown using World Stress Map (WSM) data, which is based on the web-based source application CASMO [92]. According to the map the Gulf of Gökova and its surroundings under the control of counterclockwise normal faulting, which is consistent with the result of this study.

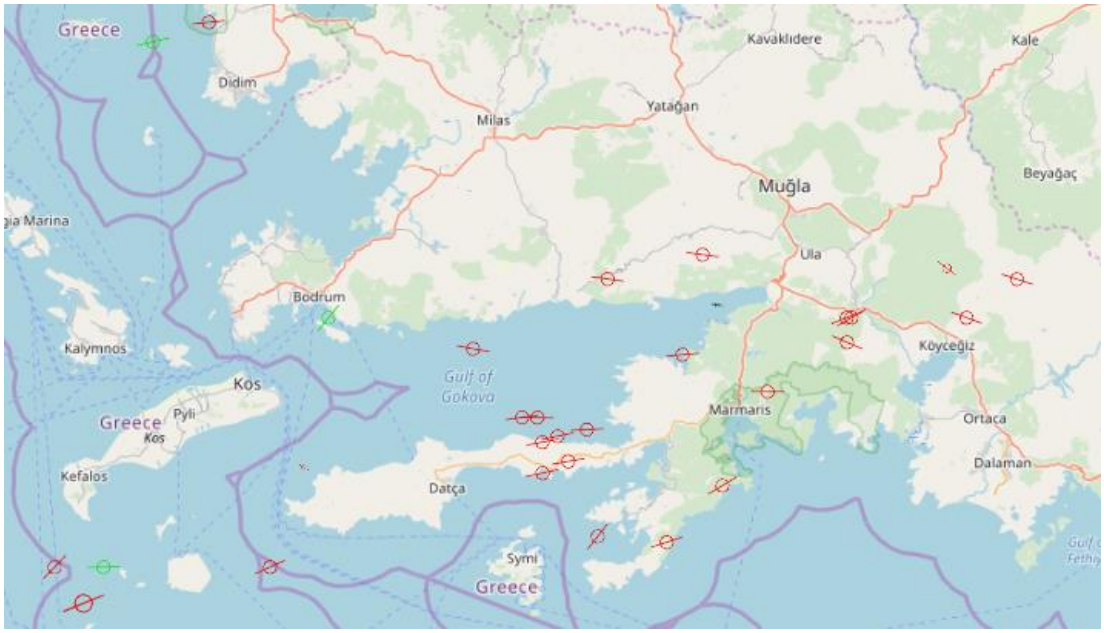


Figure 5.1: The stress map of the region. The data are taken from World Stress Map. [92] (Normal fault in red, strike-slip fault in green).

The total examination of focal mechanism solutions in the Bozburun Peninsula reveals the regime is mainly normal faulting with strike slip component that is incompatible with the previously mapped active normal faults in the area [60]. In order to conduct a more comprehensive study of this area, more data and field observations can be carried out to study the focal mechanism of the earthquakes.

According to the calculations used in this study, the region's tectonics and fault mechanisms show reasonable relationships. However, since the resulting values are obtained from specific data sources, which are only collected in a small area and for a short period of time, they have a large margin of error. The outcome should be carefully evaluated and verified using a larger data set.

# REFERENCES


[1] A. K. Tezcan, 1979, “Geothermal studies, their present status and contribution to heat flow contouring in Turkey,” in Terrestrial heat flow in Europe, pp. 283–292.

[2] M. I. Tezcan A. K. ve Turgay, 1991, “Heat flow and temperature distributions in Turkey, in Cermak, V., Haenal, R., and Zui, V., Eds., le,” Geotherm. Atlas Eur.

[3] G. Göktürkler, M. Salk, and C. Sari, 2003,“Numerical modeling of the conductive heat transfer in western Anatolia,” J. Balk. Geophys. Soc., vol. 6, no. 1, pp. 1–15.

[4] İ. Aydın, H. İ. Karat, and A. Koçak, “Curie-point depth map of Turkey,” Geophys. J. Int., vol. 162, no. 2, pp. 633–640, 2005.

[5] G. Karayel, 2009, “Bodrum TurgutReis sahillerinin doğal radyoaktivite seviyesinin belirlenmesi ve bölgenin jeolojik yapısıyla ilişklendirilmesi,” in The 5th Eurasian Conference on Nuclear Science and its Application, vol. 1, pp. 203–210.

[6] A. Uğur and Ü. Ahmet, 2013, “The Airborne Magnetic Signature of Gökova Gulf,” Bull. Miner. Res. Explor., vol. 147, no. 147, pp. 169–177.

[7] A. Uğur, E. U. ULUGERGERLİ, and S. KUTLU, “The assessment of geothermal potential of Turkey by means of heat flow estimation,” Bull. Miner. Res. Explor., vol. 149, no. 149, pp. 201–210, 2014.

[8] E. E., 2018, “Thermal Structure of The Southwest Anatolia and Correlation with the Aegean Hellenic Arc Ph.D. Thesis, Süleyman Demirel University Graduate School of Natural and Applied Sciences”.

[9] İ. Çağlar and E. Duvarci, 2001, “Geoelectric structure of inland area of the Gökova rift, southwest Anatolia and its tectonic implications,” J. Geodyn., vol. 31, no. 1, pp. 33–48.

[10] E. Düztaş et al., 2017, “Electrical Resistivity Tomography (ERT) and Induced Polarization (IP) Applied to Karst Alluvium: Case Study from Azmak Spring, Mugla, Turkey,” in Proceedings of the International Groundwater Conference.

[11] B. Günay, 1999, “Investigation of Tectonic Characteristics of Saroz, Edremit and Gökova Gulfs by Means of Seismic Reflection Data Interpretation,” Ph.D.

Thesis, İstanbul.

[12] H. Kurt, E. Demirbağ, and İ. Kuşçu, 1999, “Investigation of the submarine active tectonism in the Gulf of Gökova, southwest Anatolia–southeast Aegean Sea, by multi-channel seismic reflection data,” Tectonophysics, vol. 305, no. 4, pp. 477–496.

[13] K. N., 2004, “Investigation of neotectonism in the Southwest Anatolia by seismic data”.

[14] E. M., 2019, “Submarine tectonics and seismic stratigraphy in the Gulf of Gökova”.

[15] H. Eyidoğan, A. Akıncı, O. Gündoğdu, O. Polat, and B. Kaypak, 1996, “Investigation of the recent seismic activity of Gökova Basin,” in National Marine Geology and Geophysical Programme Workshop I, Proceedings, pp. 8–9.

[16] M. Aktar et al., 2006, “Gökova Körfezi (Muğla) Aktif Faylarında Güncel Sismik Aktivitenin Belirlenmesi,” TÜBITAK Projesi, no. 104Y336.

[17] N. Sayil and İ. Osmanşahin, “An investigation of seismicity for western Anatolia,” Nat. Hazards, vol. 44, pp. 51–64, 2008.

[18] S. Yolsal-Çevikbilen, T. Taymaz, and C. Helvacı, 2014, “Earthquake mechanisms in the Gulfs of Gökova, Sığacık, Kuşadası, and the Simav Region (western Turkey): Neotectonics, seismotectonics and geodynamic implications,” Tectonophysics, vol. 635, pp. 100–124.

[19] S. Rontogianni, K. I. Konstantinou, C. Evangelidis, and N. S. Melis, 2011, “Investigating potential Seismic Hazard in the Gulf of Gökova (South Eastern Aegean Sea) deduced from recent shallow earthquake activity,” in AGU Fall Meeting Abstracts, vol. 2011, pp. T43E-2427.

[20] N. C. A. Kılıç and Ü. Y. Kalyoncuoğlu, 2017, “Muğla İli ve çevresi için depremsellik ve sismik tehlike analizi,” Mühendislik Bilim. ve Tasarım Derg., vol. 5, no. 3, pp. 507–524.

[21] R. Andinisari, K. I. Konstantinou, and P. Ranjan, 2020, “Seismotectonics of SE Aegean inferred from precise relative locations of shallow crustal earthquakes,” J. Seismol., vol. 24, pp. 1–22.

[22] V. Vavryčuk, 2014, “Iterative joint inversion for stress and fault orientations from focal mechanisms,” Geophys. J. Int., vol. 199, no. 1, pp. 69–77.

[23] D. McKenzie, 1972, “Active tectonics of the Mediterranean region,” Geophys.

J. Int., vol. 30, no. 2, pp. 109–185.

[24] A. M. C. Sengör, 1979, “The North Anatolian transform fault: its age, offset and tectonic significance,” J. Geol. Soc. London., vol. 136, no. 3, pp. 269–282.

[25] J. F. Dewey and A. M. Cel. Şengör, 1979, “Aegean and surrounding regions: complex multiplate and continuum tectonics in a convergent zone,” Geol. Soc. Am. Bull., vol. 90, no. 1, pp. 84–92.

[26] A. M. C. Şengör, N. Görür, and F. Şaroğlu, 1985, “Strike-slip faulting and related basin formation in zones of tectonic escape: Turkey as a case study”.

[27] Y. Rotstein, 1984, “Counterclockwise rotation of the Anatolian block,” Tectonophysics, vol. 108, no. 1–2, pp. 71–91.

[28] S. Mcclusky et al., 2000, “Global Positioning System constraints on plate kinematics and dynamics in the eastern Mediterranean and Caucasus,” J. Geophys. Res. Solid Earth, vol. 105, no. B3, pp. 5695–5719.

[29] D. McKenzie, 1978,“Active tectonics of the Alpine—Himalayan belt: the Aegean Sea and surrounding regions,” Geophys. J. Int., vol. 55, no. 1, pp. 217–254.

[30] X. Le Pichon, N. Chamot-Rooke, S. Lallemant, R. Noomen, and G. Veis, 1995, “Geodetic determination of the kinematics of central Greece with respect to Europe: Implications for eastern Mediterranean tectonics,” J. Geophys. Res. Solid Earth, vol. 100, no. B7, pp. 12675–12690.

[31] X. Le Pichon and J. Angelier, 1979, “The Hellenic arc and trench system: a key to the neotectonic evolution of the eastern Mediterranean area,” Tectonophysics, vol. 60, no. 1–2, pp. 1–42.

[32] R. Şengör, A.M.C., Satır, M., Akkök, 1984, “Timing of tectonic events in the Menderes Massif, western Turkey: implications for tectonic evolution and evidence for Pan-African basement in Turkey,” Tectonics, pp. 3, 693–707.

[33] P. Reilinger, R., McClusky, S., Paradissis, D., Ergintav, S., Vernant, 2010, “Geodetic constraints on the tectonic evolution of the Aegean region and strain accumulation along the Hellenic subduction zone,” Tectonophysics, doi: doi:10.1016/j.tecto.2009.05.027.

[34] R. E. Reilinger et al., 1997,“Global Positioning System measurements of present-day crustal movements in the Arabia-Africa-Eurasia plate collision zone,” J. Geophys. Res. Solid Earth, vol. 102, no. B5, pp. 9983–9999.

[35] J. Jackson and D. McKenzie, 1988, “The relationship between plate motions and seismic moment tensors, and the rates of active deformation in the Mediterranean and Middle East,” Geophys. J. Int., vol. 93, no. 1, pp. 45–73.

[36] N. N. Ambraseys, “Engineering seismology: part II,” Earthq. Eng. Struct. Dyn., vol. 17, no. 1, pp. 51–105, 1988.

[37] T. Taymaz, J. Jackson, and D. McKenzie, 1991, “Active tectonics of the north and central Aegean Sea,” Geophys. J. Int., vol. 106, no. 2, pp. 433–490.

[38] N. N. Ambraseys and J. A. Jackson, 1998, “Faulting associated with historical and recent earthquakes in the Eastern Mediterranean region,” Geophys. J. Int., vol. 133, no. 2, pp. 390–406.

[39] H. Eyidoğan and J. Jackson, 1985, “A seismological study of normal faulting in the Demirci, Alaşehir and Gediz earthquakes of 1969–70 in western Turkey: Implications for the nature and geometry of deformation in the continental crust,” Geophys. J. Int., vol. 81, no. 3, pp. 569–607.

[40] H. Eyidoğan, 1988,“Rates of crustal deformation in western Turkey as deduced from major earthquakes,” Tectonophysics, vol. 148, no. 1–2, pp. 83–92.

[41] J. A. Jackson, G. King, and C. Vita-Finzi, 1982,“The neotectonics of the Aegean: an alternative view,” Earth Planet. Sci. Lett., vol. 61, no. 2, pp. 303–318.

[42] T. Taymaz, 1993,“The source parameters of the Çubukdağ (W. Turkey) earthquake of 1986 October 11,” Geophys. J. Int., vol. 113, no. 1, pp. 260–267.

[43] E. Bozkurt, 2001, “Neotectonics of Turkey–a synthesis,” Geodin. acta, vol. 14, no. 1–3, pp. 3–30.

[44] B. Aktug et al., 2009, “Deformation of western Turkey from a combination of permanent and campaign GPS data: Limits to block-like behavior,” J. Geophys. Res. Solid Earth, vol. 114, no. B10.

[45] A. M. C. Şengör, 1987, “Cross-faults and differential stretching of hanging walls in regions of low-angle normal faulting: examples from western Turkey,” Geol. Soc. London, Spec. Publ., vol. 28, no. 1, pp. 575–589.

[46] N. Görür et al., 1995, “Rift formation in the Gökova region, southwest Anatolia: implications for the opening of the Aegean Sea,” Geol. Mag., vol. 132, no. 6, pp. 637–650.

[47] J. E. Meulenkamp, M. J. R. Wortel, W. A. Van Wamel, W. Spakman, and E. H. Strating, 1988, “On the Hellenic subduction zone and the geodynamic evolution of Crete since the late Middle Miocene,” Tectonophysics, vol. 146, no. 1–4, pp. 203–215.

[48] X. Le Pichon and J. Angelier, 1981, “The Aegean Sea,” Philos. Trans. R. Soc. London. Ser. A, Math. Phys. Sci., vol. 300, no. 1454, pp. 357–372.

[49] C. Kissel and C. Laj, 1988, “The Tertiary geodynamical evolution of the Aegean arc: a paleomagnetic reconstruction,” Tectonophysics, vol. 146, no. 1–4, pp. 183–201.

[50] G. Seyitoğlu and B. Scott, 1991, “Late Cenozoic crustal extension and basin formation in west Turkey,” Geol. Mag., vol. 128, no. 2, pp. 155–166.

[51] G. Seyitoğlu and B. C. Scott, 1992, “The age of the Büyük Menderes graben (west Turkey) and its tectonic implications,” Geol. Mag., vol. 129, no. 2, pp. 239–242.

[52] A. M. C. Şengör and Y. Yilmaz, 1981, “Tethyan evolution of Turkey: a plate tectonic approach,” Tectonophysics, vol. 75, no. 3–4, pp. 181–241.

[53] A. Koçyiđit, H. Yusufođlu, and E. Bozkurt, 1999, “Evidence from the Gediz graben for episodic two-stage extension in western Turkey,” J. Geol. Soc. London., vol. 156, no. 3, pp. 605–616.

[54] E. Bozkurt, 2001, “Late Alpine evolution of the central Menderes Massif, western Turkey,” Int. J. Earth Sci., vol. 89, pp. 728–744.

[55] N. Sarica, 2000, “The Plio-Pleistocene age of Büyük Menderes and Gediz grabens and their tectonic significance on N-S extensional tectonics in West Anatolia: mammalian evidence from the continental deposits,” Geol. J., vol. 35, no. 1, pp. 1–24.

[56] Y. Yilmaz et al., 2000, “When did the western Anatolian grabens begin to develop?,” Geol. Soc. London, Spec. Publ., vol. 173, no. 1, pp. 353–384.

[57] F. Şaroglu, Ö. Emre, and I. Kuşcu, 1995, “Türkiye diri fay haritasi,” MTA Int. Rep.

[58] A. Uluğ, M. Duman, M. Avcı, and E. Özel, 1996, “Late Quaternary evolution of the Gulf of Gökova, Southeastern Agean Sea: deltaic sedimentation and sea level,” in 11th Petroleum Congress of Turkey Proceedings Book, pp. 59–72.

[59] F. Şaroğlu, Ö. Emre, and İ. Kuşçu, 1992, “Active fault map of Turkey,” Gen. Dir. Miner. Res. Explor. Ankara, Turkey, vol. 2.

[60] Ş. F. Emre Ö, Duman TY, Özalp S, Elmacı H, Olgun Ş, 2013, "Active Fault Map of Turkey with and Explanatory Text 1:1,250,000 scale," Gen. Dir. Miner.

[61] Ö. Emre, T. Y. Duman, S. Özalp, H. Elmaci, and S. Olgun, 2011, "1: 250,000 scale active fault map series of Turkey," Kayseri (NJ36-8) Quadrange, Ankara.

[62] Ö. F. Gürer, E. Sanğu, M. Özburan, A. Gürbüz, and N. Sarica-Filoreau, 2013, "Complex basin evolution in the Gökova Gulf region: implications on the Late Cenozoic tectonics of southwest Turkey," Int. J. Earth Sci., vol. 102, pp. 2199–2221.

[63] M. Basmenji, H. S. Akyüz, E. Kirkan, M. E. Aksoy, G. Uçarkuş, and N. Yakupoğlu, 2021, "Earthquake history of the Yatağan Fault (Muğla, SW Turkey): implications for regionalseismic hazard assessment and paleoseismology in extensional provinces," Turkish J. Earth Sci., vol. 30, no. 2, pp. 161–181.

[64] M. Akyüz, S., Aksoy, ME., Uçarkuş, G., Akyüz-Dikbaş, A., Kırkan, E., Basmenji, 2019, "Muğla, Yatağan, Milas ve Gökova Faylarının morfotektonik, paleosismolojik ve kinematik özellikleri".

[65] V. Karabacak, 2016, "Seismic damage in the Lagina sacred area on the Mugla Fault: a key point for the understanding of the obliquely situated faults of western Anatolia," J. Seismol., vol. 20, pp. 277–289.

[66] A. Uluğ, M. Duman, Ş. Ersoy, E. Özel, and M. Avcı, 2005, "Late Quaternary sea-level change, sedimentation and neotectonics of the Gulf of Gökova: Southeastern Aegean Sea," Mar. Geol., vol. 221, no. 1–4, pp. 381–395.

[67] Y. İşcan, H. Tur, and E. Gökaşan, 2013, "Morphologic and seismic features of the Gulf of Gökova, SW Anatolia: evidence of strike-slip faulting with compression in the Aegean extensional regime," Geo-Marine Lett., vol. 33, pp. 31–48.

[68] H. Tur, C. Yaltırak, İ. Elitez, and K. T. Sarıkavak, 2015, "Pliocene–Quaternary tectonic evolution of the Gulf of Gökova, southwest Turkey," Tectonophysics, vol. 638, pp. 158–176.

[69] N. Ocakoğlu, P. Nomikou, Y. İşcan, M. F. Loreto, and D. Lampridou, 2018, "Evidence of extensional and strike-slip deformation in the offshore Gökova-Kos area affected by the July 2017 Mw6. 6 Bodrum-Kos earthquake, eastern

Aegean Sea," Geo-Marine Lett., vol. 38, pp. 211–225.

[70] E. Karasözen et al., 2018, "The 2017 July 20 M w 6.6 Bodrum–Kos earthquake illuminates active faulting in the Gulf of Gökova, SW Turkey," Geophys. J. Int., vol. 214, no. 1, pp. 185–199.

[71] A. Ganas et al., 2019, "The July 20, 2017 M6. 6 Kos earthquake: seismic and geodetic evidence for an active north-dipping normal fault at the western end of the Gulf of Gökova (SE Aegean Sea)," Pure Appl. Geophys., vol. 176, pp. 4177–4211.

[72] S. Sboras, I. Lazos, E. Mouzakiotis, V. Karastathis, S. Pavlides, and A. Chatzipetros, 2020, "Fault modelling, seismic sequence evolution and stress transfer scenarios for the July 20, 2017 (MW 6.6) Kos–Gökova Gulf earthquake, SE Aegean," Acta Geophys., vol. 68, pp. 1245–1261.

[73] İ. Tiryakioğlu et al., 2018, "Slip distribution and source parameters of the 20 July 2017 Bodrum-Kos earthquake (Mw6. 6) from GPS observations," Geodin. Acta, vol. 30, no. 1, pp. 1–14.

[74] G. Papadopoulos et al., 2019, "Fault models for the Bodrum–Kos tsunamigenic earthquake (Mw6. 6) of 20 July 2017 in the east Aegean Sea," J. Geodyn., vol. 131, p. 101646.

[75] N. Ambraseys, 2009, Earthquakes in the Mediterranean and Middle East: a multidisciplinary study of seismicity up to 1900. Cambridge University Press.

[76] S. Stein, M. Wysession, and H. Houston, 2003, "Books-An Introduction to Seismology, Earthquakes, and Earth Structure," Phys. Today, vol. 56, no. 10, pp. 65–72.

[77] K. Aki and P. G. Richards, 2002, Quantitative seismology.

[78] M. L. u Jost and R. B. Herrmann, 1989, "A student's guide to and review of moment tensors," Seismol. Res. Lett., vol. 60, no. 2, pp. 37–57.

[79] A. Barth, 2007, "Frequency sensitive moment tensor inversion for light to moderate magnitude earthquakes in eastern Africa and derivation of the regional stress field." Karlsruhe, Univ., Diss.

[80] R. B. Herrmann, 2013, "Computer programs in seismology: An evolving tool for instruction and research," Seismol. Res. Lett., vol. 84, no. 6, pp. 1081–1088.

[81] J. Angelier, 1979, "Determination of the mean principal directions of stresses for a given fault population," Tectonophysics, vol. 56, no. 3–4, pp. T17–T26.

[82] J. Angelier, 1984, “Tectonic analysis of fault slip data sets,” J. Geophys. Res. Solid Earth, vol. 89, no. B7, pp. 5835–5848.

[83] A. Jacques, 2002, “Inversion of earthquake focal mechanisms to obtain the seismotectonic stress IV—a new method free of choice among nodal planes,” Geophys. J. Int., vol. 150, no. 3, pp. 588–609.

[84] J. W. Gephart and D. W. Forsyth, 1984, “An improved method for determining the regional stress tensor using earthquake focal mechanism data: application to the San Fernando earthquake sequence,” J. Geophys. Res. Solid Earth, vol. 89, no. B11, pp. 9305–9320.

[85] A. J. Michael, 1984, “Determination of stress from slip data: faults and folds,” J. Geophys. Res. Solid Earth, vol. 89, no. B13, pp. 11517–11526.

[86] A. J. Michael, 1987, “Use of focal mechanisms to determine stress: a control study,” J. Geophys. Res. Solid Earth, vol. 92, no. B1, pp. 357–368.

[87] J. W. Gephart, 1990, “Stress and the direction of slip on fault planes,” Tectonics, vol. 9, no. 4, pp. 845–858.

[88] L. Rivera and A. Cisternas, 1990, “Stress tensor and fault plane solutions for a population of earthquakes,” Bull. Seismol. Soc. Am., vol. 80, no. 3, pp. 600–614.

[89] D. Delvaux and B. Sperner, 2003, “Stress tensor inversion from fault kinematic indicators and focal mechanism data: the TENSOR program,” New insights into Struct. Interpret. Model., vol. 212, pp. 75–100.

[90] R. Arnold and J. Townend, 2007, “A Bayesian approach to estimating tectonic stress from seismological data,” Geophys. J. Int., vol. 170, no. 3, pp. 1336–1356.

[91] M. Lou Zoback, 1992, “Stress field constraints on intraplate seismicity in eastern North America,” J. Geophys. Res. Solid Earth, vol. 97, no. B8, pp. 11761–11782.

[92] A. Barth, J. Reinecker, and O. Heidbach, 2008, “Stress derivation from earthquake focal mechanisms,” World Stress Map Proj. Guidel., vol. 12, pp. 1–12.

# BIOGRAPHY

Edanur TANÜLKÜ AL JASIM works as a research assistant at Gebze Technical University Earth and Marine Sciences Institute. She received her BSc in Geophysical Engineering in 2014 from Ankara University, Ankara, Turkey, and she is currently a MSc student on Earth Sciences at Gebze Technical University Earth and Marine Sciences Institute, Turkey.

# APPENDICES

## Appendices A: Publishments produced by the thesis study.

Tanülkü Al Jasım E., Acarel D., Kaypak B. (2022). Gökova Körfezi ve Yakın Çevresinin Deprem Odak Mekanizması Analizi. Lisansüstü Araştırmalar Sempozyumu. 01-02/06/2022. Kocaeli.